



Lithospheric structure in the Baikal–central Mongolia region from integrated geophysical-petrological inversion of surface-wave data and topographic elevation

J. Fulla

Dublin Institute for Advanced Studies, 5 Merrion Square, Dublin 2, Ireland

Now at Institute of Geosciences, CSIC-UCM, ES-28040 Madrid, Spain (j.fulla@igeo.ucm-csic.es)

S. Lebedev, M. R. Agius, and A. G. Jones

Dublin Institute for Advanced Studies, 5 Merrion Square, Dublin 2, Ireland

J. C. Afonso

ARC Centre of Excellence for Core to Crust Fluid Systems, GEMOC, Department of Earth and Planetary Sciences, Macquarie University, Sydney, New South Wales 2109, Australia

[1] Recent advances in computational petrological modeling provide accurate methods for computing seismic velocities and density within the lithospheric and sub-lithospheric mantle, given the bulk composition, temperature, and pressure within them. Here, we test an integrated geophysical-petrological inversion of Rayleigh- and Love-wave phase-velocity curves for fine-scale lithospheric structure. The main parameters of the grid-search inversion are the lithospheric and crustal thicknesses, mantle composition, and bulk density and seismic velocities within the crust. Conductive lithospheric geotherms are computed using P-T-dependent thermal conductivity. Radial anisotropy and seismic attenuation have a substantial effect on the results and are modeled explicitly. Surface topography provides information on the integrated density of the crust, poorly constrained by surface waves alone. Investigating parameter inter-dependencies, we show that accurate surface-wave data and topography can constrain robust lithospheric models. We apply the inversion to central Mongolia, south of the Baikal Rift Zone, a key area of deformation in Asia with debated lithosphere-asthenosphere structure and rifting mechanism, and detect an 80–90 km thick lithosphere with a dense, mafic lower crust and a relatively fertile mantle composition ($Mg\# < 90.2$). Published measurements on crustal and mantle Miocene and Pleistocene xenoliths are consistent with both the geotherms and the crustal and lithospheric mantle composition derived from our inversion. Topography can be fully accounted for by local isostasy, with no dynamic support required. The mantle structure constrained by the inversion indicates no major thermal anomalies in the shallow sub-lithospheric mantle, consistent with passive rifting in the Baikal Rift Zone.

Components: 12,200 words, 9 figures, 3 tables.

Keywords: Baikal Rift; lithosphere-asthenosphere boundary; mantle composition; petro-physical modeling; surface wave.

Index Terms: 1212 Geodesy and Gravity: Earth's interior: composition and state (7207, 7208, 8105, 8124); 3610 Mineralogy and Petrology: Geochemical modeling (1009, 8410); 7255 Seismology: Surface waves and free oscillations.

Received 7 March 2012; **Revised** 14 June 2012; **Accepted** 15 June 2012; **Published** 7 August 2012.

Fullea, J., S. Lebedev, M. R. Agius, A. G. Jones, and J. C. Afonso (2012), Lithospheric structure in the Baikal–central Mongolia region from integrated geophysical-petrological inversion of surface-wave data and topographic elevation, *Geochem. Geophys. Geosyst.*, 13, Q0AK09, doi:10.1029/2012GC004138.

Theme: The Lithosphere-Asthenosphere Boundary

1. Introduction

[2] The thermal and compositional structure of the lithosphere-asthenosphere system holds essential keys to our understanding of the dynamics and evolution of the lithosphere, the nature of the coupling between the lithosphere and the sub-lithospheric upper mantle, and the relationship between the Earth's surface features and deep seated processes. The physical properties of the lithosphere can be inferred from seismic observations, as seismic velocities within the lithosphere depend on the temperature, pressure and composition of the rocks at depth [e.g., Afonso *et al.*, 2008; Cammarano *et al.*, 2003; Duffy and Anderson, 1989; Goes *et al.*, 2000; Stixrude and Lithgow-Bertelloni, 2005].

[3] The lithosphere-asthenosphere boundary (LAB) separates the outermost, cold, relatively rigid layer of the Earth (lithosphere) from the warmer, rheologically weaker sub-lithospheric mantle. It has been proposed that the asthenosphere, in contrast to the lithosphere, may undergo widespread partial melting, or contain much more water than the lithosphere [e.g., Anderson and Sammis, 1970; Hirth and Kohlstedt, 1996; Karato, 2012; Kawakatsu *et al.*, 2009; Schmerr, 2012]. The depth and sharpness of the LAB have been investigated using various proxies: changes in seismic velocity, seismic radial anisotropy, electrical resistivity, composition and temperature [e.g., Deschamps *et al.*, 2008; Eaton *et al.*, 2009; Endrun *et al.*, 2011; Fischer *et al.*, 2010; Gung *et al.*, 2003; Kind *et al.*, 2012; Muller *et al.*, 2009; Plomerová *et al.*, 2002; Rychert and Shearer, 2009; Romanowicz, 2009; Yuan and Romanowicz, 2010]. In this paper, we first adopt a LAB definition based primarily on the distribution of temperature with depth, and then discuss the implications of our results for the seismic visibility of the LAB.

[4] Seismic surface waves are particularly sensitive to the structure of the lithosphere. Inversions of surface-wave measurements have long been used in order to constrain the shear-velocity structure, thickness and thermal state of the lithosphere [e.g., Boschi *et al.*, 2010; Brune and Dorman, 1963; Lebedev *et al.*, 2009; Priestley and McKenzie,

2006; Shapiro and Ritzwoller, 2004]. Surface waves at different periods sample the crust and upper mantle differently, with longer periods being more sensitive to deeper structure (see auxiliary material).¹ Accurate surface-wave phase-velocity curves extending over a broad period range have substantial sensitivity to the depth of the shear-speed reduction near the bottom of the lithosphere [Bartzsch *et al.*, 2011]. However, they are weakly sensitive to the width and the fine structure of the LAB, which contributes to the non-uniqueness of seismic-velocity and thermal models inferred from surface-wave inversions. Introduction of a priori constraints into seismic data inversions has been used as one way to reduce the non-uniqueness and narrow down the ranges of acceptable models [Deal and Nolet, 1996; Shapiro and Ritzwoller, 2004].

[5] Surface waves are less sensitive to density than they are to seismic velocities at depth. In order to constrain the density distribution within the lithosphere, inversions of surface-wave data need to incorporate additional information such as surface topography.

[6] The advantages of combining potential fields, topography and seismic data to image the Earth's interior have been recognized by several authors [e.g., Deschamps *et al.*, 2002; Forte and Perry, 2000; Forte *et al.*, 2010; Perry *et al.*, 2003; Simmons *et al.*, 2010]. Integrated geophysical-petrological modeling of physical properties of the rocks at depth — and, from those, of different geophysical observables — offers a way to combine different data sets into a single, unified, internally consistent framework [e.g., Afonso *et al.*, 2008; Cammarano *et al.*, 2009; Connolly, 2005; Fullea *et al.*, 2010, 2011; Khan *et al.*, 2009, 2011], reducing the uncertainties associated with modeling the observables separately. Importantly, errors associated with the geophysical-petrological modeling itself (including those due to uncertainties in mantle composition and seismic attenuation or radial anisotropy) must now be evaluated. If these errors can be taken into

¹Auxiliary materials are available in the HTML. doi:10.1029/2012GC004138.

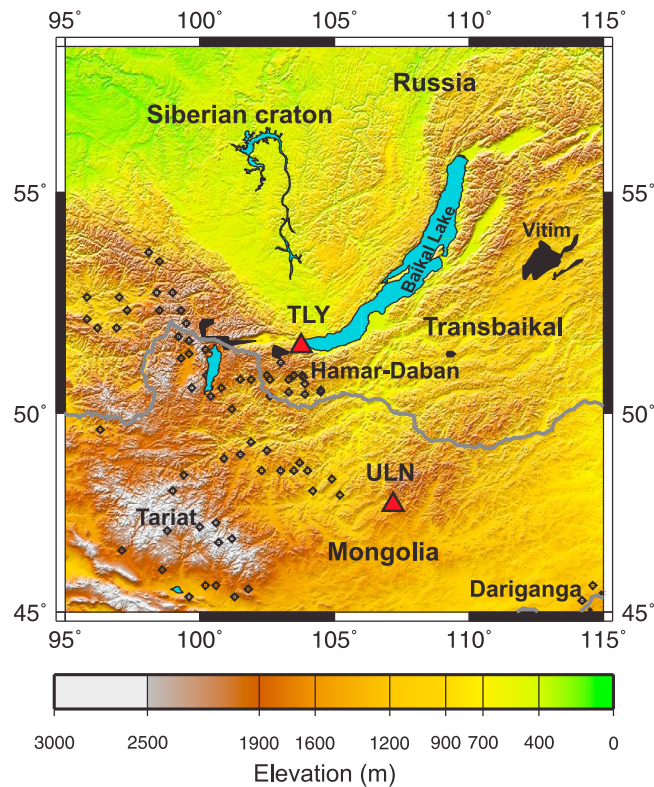


Figure 1. Baikal–central Mongolia region. The surface-wave dispersion curves used in our analysis are averages along the corridor between seismic stations Talaya (TLY) and Ulaanbaatar (ULN), depicted as red triangles. Cenozoic volcanic fields [Kiselev, 1987] are shown as black areas.

account, and if sufficiently accurate data are available, then the integrated modeling can reproduce the lithospheric geotherms with high radial resolution, while also constraining the density and composition of the crust and mantle.

[7] In this paper, we test a coupled geophysical-petrological inversion of fundamental-mode, Rayleigh- and Love-wave dispersion curves and topography data, with supplementary constraints from surface heat flow, crustal seismic models and xenolith data, for one-dimensional structural profiles. The signal of the lithosphere-asthenosphere structure in phase-velocity data is very subtle [Bartzsch *et al.*, 2011]. An accuracy of a few tenths of per cent in the phase velocity value is required in both the measurements and the inversion. Currently, sufficiently accurate surface-wave measurements are becoming increasingly available. The focus of this paper is on the relationship between data and the physical structure of the lithosphere. We examine in detail the factors that affect the accuracy of the data-model relationship, including uncertainties in attenuation, radial anisotropy and mantle composition, and introduce,

as a proof of concept, a simple grid-search inversion of surface-wave data for the thermal and compositional structure of the lithosphere.

2. Baikal–Central Mongolia Region

2.1. Geological Background

[8] Central Mongolia is located south of the Archaen-Paleoproterozoic Siberian Craton and the continental Baikal Rift Zone (Figure 1). Central Mongolia and the Transbaikalian domains were formed by the Phanerozoic assemblage of different terrains (Precambrian micro continents, island arcs, continental marginal basins and oceanic crust) and now undergo moderate active deformation, likely related to the India-Eurasia collision [e.g., Calais *et al.*, 2003].

[9] The nature of the neighboring Baikal Rift Zone has been characterized as either “active” or “passive,” according to different interpretations of geological and geophysical observations [e.g., Sengör and Burke, 1978]. Authors in favor of the “active”

Table 1. Bulk Mantle Compositions Used in This Study

	Composition 1: Av. Central Mongolia and Baikal ^a (wt%)	Composition 2: Dariganga ^a (wt%)	Composition 3: Siberia-Yakutia ^b (sp and gnt) (wt%)	Composition 4: Siberia-Udachnaya ^c (gnt) (wt%)	Composition 5: Siberia-Udachnaya ^c (sp) (wt%)	Composition 6: PUM M&S95 ^d (wt%)
SiO ₂	44.59	44.44	42.87	43.94	43.94	45
TiO ₂	0.14	0.06	–	0.06	0.02	0.201
Al ₂ O ₃	3.48	2.3	1.44	1.31	0.95	4.45
Cr ₂ O ₃	0.4	0.38	0.41	0.4	0.34	0.384
FeO	8.25	8.09	8.19	7.54	6.78	8.05
MnO	0.14	0.13	0.13	0.15	0.12	0.135
MgO	39.56	42.04	45.29	45.02	45.61	37.8
CaO	2.85	2.05	1.23	1.08	0.76	3.55
Na ₂ O	0.31	0.22	0.06	0.07	0.06	0.36
NiO	0.26	0.28	0.27	0.33	0.32	–
Total	99.98	100	99.9	99.9	99.88	99.93
Mg#	89.7	90.2	90.8	91.4	92.3	89.3

^aCentral Mongolia–Baikal and Dariganga composition come from *Ionov* [2002, and references therein].

^bGarnet and spinel peridotite average in Yakutia (Siberia) from *Ukhanov et al.* [1988].

^cUdachnaya data from *Boyd et al.* [1997].

^dPUM stands for Primitive Upper Mantle, M&S95 refers to *McDonough and Sun* [1995].

hypothesis suggest, on the basis of the interpretation of gravity, deep seismic data and tomography models, the existence of a large scale mantle upwelling that gives rise to a thermal anomaly beneath and near the rift axis [e.g., *Gao et al.*, 2003; *Logatchev and Zorin*, 1987; *Zhao et al.*, 2006; *Zorin*, 1981]. Those in favor of the “passive” model invoke, on the basis of the interpretation of similar data sets, passive and localized sub-lithospheric upwelling driven by tectonic, plate-scale forces [e.g., *Molnar and Tapponnier*, 1975; *Petit and Déverchère*, 2006; *Ruppel*, 1995; *Tiberi et al.*, 2003] in the context of inherited weak lithospheric zones and the strong and cold Siberian Craton [*Burov et al.*, 1994]. Here, we apply our integrated geophysical-petrological analysis in order to constrain the lithospheric architecture and determine whether a lithospheric or uppermost sub-lithospheric mantle thermal anomaly is present in the vicinity of the Baikal Rift.

[10] The volcanism in Mongolia and the Transbaikal area comprises mainly alkali olivine basalts with subordinate olivine tholeiites and basanites. The volcanic fields are characterized by the relatively low volume erupted, a widespread spatial pattern (Figure 1), and the lack of age progression within the volcanic provinces [e.g., *Barry et al.*, 2003; *Ionov*, 2002]. Mantle xenoliths from basaltic volcanic areas in Mongolia typically include medium- to coarse-grained spinel and garnet lherzolites with relatively fertile major-element compositions (i.e., Mg# = 89.7–90.2, see Table 1) [e.g., *Barry et al.*, 2003; *Ionov*, 2002]. In contrast, xenoliths from kimberlite pipes within the Siberian Platform show a relatively depleted composition (i.e., Mg# = 90.8–

92.3, see Table 1) [*Boyd et al.*, 1997; *Ukhanov et al.*, 1988].

2.2. Geophysical Background

[11] Regional, broadband, phase-velocity curves for central Mongolia — for both Rayleigh and Love surface waves — are available from *Lebedev et al.* [2006], who measured them as averages along a corridor between two stations of the Global Seismographic Network: Talaya (TLY) and Ulaanbaatar (ULN) (Figure 1). The topography along a profile from TLY to ULN varies from 600 m to 2000 m with an average value of 1140 m and a standard deviation of 285 m (ETOPO2 Global Data Base (V9.1) [*Smith and Sandwell*, 1994, 1997]). The measured surface heat flow (SHF) in Central Mongolia ranges from 50 mW/m² to 60 mW/m² [*Khutorskoy and Yarmoluk*, 1989; *Lysak*, 1984; *Lysak and Dorofeeva*, 2003], disregarding local anomalies related to hydrothermal circulation [*Poort and Klerkx*, 2004]. The crust-mantle discontinuity is the major lithospheric boundary for density and seismic velocities and, therefore, constraining its depth is particularly important for the accurate modeling of topography and surface-wave dispersion curves. Seismic refraction and receiver function data can be used to constrain the *P*-wave velocity distribution in the crust and the crustal thickness. Moho depth in the central Mongolia-Lake Baikal region, according to these studies, is 41–50 km [e.g., *Gao et al.*, 2004; *Nielsen and Thybo*, 2009; *ten Brink and Taylor*, 2002; *Zorin et al.*, 2002]. *P*-wave velocity in the vicinity of Lake Baikal is 6.0–6.2 km/s, 6.5–6.7 km/s and 7.2–

7.3 km/s in the upper, middle and lower crust, respectively, according to seismic refraction data [Nielsen and Thybo, 2009].

3. Integrated Geophysical-Petrological Inversion

[12] We set up a petro-physically driven grid-search inversion scheme based on the software package LitMod [Afonso *et al.*, 2008; Fullea *et al.*, 2009]. This software combines petrological and geophysical modeling of the lithosphere and sub-lithospheric upper mantle within an internally consistent thermodynamic-geophysical framework. In this study we assume that the lithospheric mantle is characterized: i) thermally, as the portion of the mantle defined by a conductive geotherm, and ii) compositionally, as the portion of the mantle characterized by a generally different (normally, more depleted) composition with respect to the fertile primary composition in the sub-lithosphere (i.e., PUM in Table 1).

3.1. The Inversion

[13] We invert simultaneously the phase-velocity curves of fundamental-mode Rayleigh and Love waves and topography data for lithospheric structure. The model parameters are the Moho and LAB depths, the bulk composition of the lithospheric mantle, and the density and S -wave velocity profiles within the crust. Radiogenic heat production in the crust and mantle, and the thermal conductivity and V_p in the crust are all fixed parameters.

[14] Fundamentally, the geotherm is the main common link between topography and surface-wave data, allowing us to couple the inversion of these data sets. The inversion is set up as a three-step, grid-search algorithm in which the forward problem (see section 3.2) is solved recurrently: i) first, the model space (given by the Moho and LAB depths, mantle composition and the density and S -wave velocity in the crust) is explored so as to find ranges of parameter values that minimize the misfit for Rayleigh and Love waves and topography data, assuming an initial radial anisotropy distribution (pre-computed in a purely seismic inversion of Love and Rayleigh dispersion curves); ii) second, keeping constant the density distributions and the Moho depth obtained in the previous step, the Levenberg-Marquardt nonlinear gradient search is applied to invert the Rayleigh- and Love-wave dispersion data for an updated, optimal radial anisotropy profile (see

section 4.3); iii) finally, model space around the best fitting ranges is explored as in the first step, now assuming the optimal radial anisotropy from the previous step. The special, iterative treatment of anisotropy is introduced in order to speed up the inversion.

3.2. The Forward Problem

[15] Our forward problem comprises two steps: i) determination of the distributions of temperature and density with depth; and ii) computation of Rayleigh- and Love-wave phase-velocity curves, topography. The geotherms are computed under the assumption of steady state heat transfer in the lithospheric mantle, using a P-T-dependent thermal conductivity [Afonso *et al.*, 2008; Fullea *et al.*, 2009]. In the crust, we assume constant, uniform values for the radiogenic heat production and thermal conductivity. Between the lithosphere and sub-lithospheric mantle we postulate a buffer layer with a variable thickness and a superadiabatic temperature gradient within it (i.e., heat transfer is controlled by conduction and convection [e.g., Fullea *et al.*, 2009]). The rationale for the buffer layer is to simulate the thermal effect of a rheologically active layer at the bottom of the upper thermal boundary layer in the convecting mantle [Solomatov and Moresi, 2000; Zaranek and Parmentier, 2004]. In the buffer zone, the temperature varies linearly from the value at the bottom of the lithosphere ($T_a = 1315^\circ\text{C}$ in this study) to a temperature $T_{buffer} = 1400^\circ\text{C}$ at the bottom of the buffer layer. For $T \geq 1315^\circ\text{C}$, convective heat transport processes in the mantle grow in importance relative to heat conduction [e.g., Zlotnik *et al.*, 2008; Ballmer *et al.*, 2011]. The thickness of the transition layer, Δz_{buffer} , is allowed to vary, so as to maintain the balance between the (assumed) constant basal heat input at the bottom of the model ($z_{bot} = 400$ km depth), internal heat generation, and surface heat release in the system (surface heat flow). This ensures consistency with the reference, mid-ocean ridge (MOR) adiabatic temperature profiles and mantle convection models [Solomatov and Moresi, 2000; Zaranek and Parmentier, 2004]. Below the buffer layer the adiabatic temperature gradient is computed according to:

$$\left. \frac{dT}{dz} \right|_{adiab} = \frac{T_{bot} - T_{buffer}}{z_{bot} - (z_L + \Delta z_{buffer})}, \quad (1)$$

where z_L is the depth to the T_a isotherm. T_{bot} is the temperature at the bottom of the model ($z_{bot} =$

400 km), normally assumed to be constant and equal to 1520 C. This estimate is based on high-pressure and high-temperature phase equilibrium experiments in the system (Mg, Fe)₂SiO₄ [e.g., *Frost, 2003; Frost and Dolejš, 2007; Katsura et al., 2004*], and is consistent with potential temperatures at MORs and the global average depth of the 410-km discontinuity [*Afonso et al., 2008*, and references therein]. However, the gradient of equation (1) is forced to be in the range 0.35–0.6 C/km. This condition is not satisfied in the case of very thick (>160 km) or thin (<60 km) lithospheres and in these cases T_{bot} is allowed to vary so as to keep the thermal gradient within the range. This condition typically translates into maximum lateral temperature variations at 400 km depth of ~120 C, in agreement with predictions from seismic observations regarding the topography of the 410-km discontinuity [e.g., *Afonso et al., 2008; Chambers et al., 2005; Lebedev et al., 2003*, and references therein].

[16] In the mantle, stable mineral assemblages are computed according to a Gibbs free energy minimization strategy as described by *Connolly* [2005]. The composition of the mantle is defined in terms of its major-element composition in the NFCMAS system (Na₂O-FeO-CaO-MgO-Al₂O₃-SiO₂). All the stable assemblages in this study are computed using a modified/augmented version of the *Holland and Powell's* [1998] thermodynamic database [*Afonso and Zlotnik, 2011*]. The compositions derived from xenolith analyses usually contain extra oxides (in small proportions), in addition to those of the six-oxide system (NFCMAS) assumed here (Table 1). Before computing the Gibbs free energy minimization we recast the amounts of the six oxides for them to add to 100%, so as to use xenolith-derived compositions consistently.

[17] The predicted surface elevation is calculated by integrating the crustal and mantle densities over a 400-km-thick column (400 km down from the surface), assuming local isostasy. Dynamic contributions to elevation from sub-lithospheric loads that could arise from convection currents are not explicitly considered in this work [*Fullea et al., 2009*]. Local isostasy is generally a reasonable first-order assumption, particularly if the area over which the average topography is being computed is large enough (Figure 1). The possible consequences of a dynamic component in the observed topography are briefly discussed in section 4.5. Local isostasy implies that the mass per unit area of any lithospheric column are the same at a certain depth (the compensation level) [e.g., *Turcotte and Schubert, 2002*]. If dynamic sub-lithospheric loads

are neglected, then the compensation level can be placed at any depth below the base of the deepest lithospheric column [*Lachenbruch and Morgan, 1990*]. Following *Afonso et al.* [2008] we assume that this level coincides with the base of the numerical domain (400 km depth). The rationale for this choice is twofold: i) it covers the whole range of estimated lithospheric thicknesses, and ii) a unique global compensation level requires only a single calibration constant [see *Fullea et al., 2009*, Appendix C1]. Seismic velocities in the mantle (initially, anharmonic and isotropic) are determined according to the elastic moduli of each end-member mineral and the density of the bulk rock, as described by *Connolly and Kerrick* [2002].

[18] Anelasticity effects are of primary importance in the inversion of seismic data, particularly at high temperatures [e.g., *Cammarano et al., 2003; Goes et al., 2000; Afonso et al., 2010; Karato, 1993; Sobolev et al., 1996*]. Radial anisotropy, i.e., the difference between the horizontally and vertically polarized shear speeds, also needs to be considered so as to isolate the relationship of seismic velocities to temperature and composition — of interest here — from the effects of anisotropic fabric on the velocities; in order to determine and remove the effect of radial anisotropy, both Rayleigh and Love dispersion curves have to be inverted simultaneously [e.g., *Gung et al., 2003; Lebedev et al., 2006; Montagner, 2007*]. We compute both anelasticity and radial anisotropy as corrections to the anharmonic and isotropic output velocities. Anelastic velocities are calculated from the high-frequency anharmonic velocities according to the expressions [e.g., *Afonso et al., 2005; Karato, 1993; Minster and Anderson, 1981*]:

$$\begin{aligned}
 V_P &= V_{P0} \left(1 - \left(\frac{2}{9} \right) \cot \left(\frac{\pi\alpha}{2} \right) Q_S^{-1} \right) \\
 V_S &= V_{S0} \left(1 - \left(\frac{1}{2} \right) \cot \left(\frac{\pi\alpha}{2} \right) Q_S^{-1} \right) \\
 Q_S^{-1} &= A \left[\frac{T_0}{d} \exp \left(\frac{-(E + PV^*)}{RT} \right) \right]^\alpha
 \end{aligned} \tag{2}$$

where $Q_P = (9/4)Q_S$ is assumed (this is equivalent to assuming an infinite quality factor for the bulk modulus, i.e., $Q_K^{-1} \sim 0$). V_{P0} and V_{S0} are the unrelaxed anharmonic velocities at a given temperature (T) and pressure (P) for a given bulk composition, $A = 750 \mu\text{m}^\alpha \text{s}^{-\alpha}$, $\alpha = 0.26$, $E = 424 \text{ kJ/mol}$, R is the universal gas constant, d is the grain size, V^* the activation volume, and T_0 the reference oscillation period [*Faul and Jackson, 2005; Jackson et al.,*

Table 2. Fixed Properties and Thicknesses of the Crustal and Mantle Layers Used in This Study^a

Layer	<i>P</i> -Wave Velocity ^b (km/s)	Heat Prod. ($\mu\text{W/m}^3$)	Therm. Cond. (W/m K)	Depth of Base (km)
Uppermost crust	5.95 (± 0.05)	1	2.5	10
Mid-upper crust	6.1 (± 0.1)	0.5	2.5	20
Mid crust	6.6 (± 0.1)	0.2	2.5	33
Lower crust	7.25 (± 0.05)	0.2	2.1	***
Lithosphere mantle	composition 1*	0.02	**	***
Sub-lithosphere	composition 2*	0.02	**	400

^aAsterisk indicates that mantle densities and seismic velocities are calculated as a function of temperature, pressure and bulk composition, see the text for further details. Mantle compositions 1 and 2 are shown in Table 1. Two asterisks indicate that the thermal conductivity in the mantle varies with temperature and pressure [Fullea *et al.*, 2009]. Three asterisks indicate that the Moho and LAB depths are free parameters in the inversion.

^bValues of V_p come from Nielsen and Thybo [2009]. Values within parentheses are the uncertainties.

2002]. For this study we assume $T_0 = 50$ s, an average grain size in the upper mantle of 10 mm and $V^* = 16 \text{ cm}^3 \text{ mol}^{-1}$. We analyze the impact of assuming different values for these two parameters in section 4.4. The effects of melt or water content on seismic attenuation are not considered in this study.

[19] Radial anisotropy, R_{an} , is defined as:

$$R_{an} = \frac{V_{SH} - V_{SV}}{V_S} \quad (3)$$

$$V_S = \frac{2V_{SV} + V_{SH}}{3}$$

where V_{SV} and V_{SH} are velocities of the vertically and horizontally polarized, attenuated *S* waves, respectively, and V_S is the Voigt isotropic average. V_P is assumed to be isotropic.

[20] The synthetic, phase-velocity curves for Rayleigh and Love waves are computed from the profiles of seismic velocities (i.e., attenuated V_P and the vertically and horizontally polarized, attenuated V_S , according to equations (2) and (3)), density and shear Q using a version of the MINEOS modes code (Masters, <http://geodynamics.org/cig/software/mineos>). Below 410 km depth, the reference model AK135 is assumed for all the parameters [Kennett *et al.*, 1995]. So as to minimize the impact of uncertainties in the Q profile on the accuracy of the V_S – phase-velocity relationship, our seismic velocity profiles have a reference period of 50 s, a value approximately in the middle of the frequency range used in this study [Lebedev and van der Hilst, 2008; Liu *et al.*, 1976].

3.3. A Note on the Method: Assumptions and Limitations

[21] Four main methodological assumptions are made in this work: i) the thermal parameters in the crust (heat production and thermal conductivity) are fixed; ii) the temperature at the base of the thermal lithosphere (conductive domain) is fixed

($T_a = 1315^\circ\text{C}$); iii) the temperature distribution in the sub-lithospheric mantle is simply parameterized by a linear transition zone linking the base of the lithosphere to the adiabatic mantle; and iv) seismic attenuation, which modifies the relationship between temperature and V_S , is described by equation (2), assuming thermodynamic equilibrium. These assumptions allow us to define a simplified parameter space comprising the Moho and LAB depths, the density and V_S distributions in the crust, and the bulk composition in the lithospheric mantle characterized by its Mg#. This restricted parameter space is then sampled by means of a grid search. We do not attempt a full inversion for the mantle composition (e.g., wt% of the main oxides in the NCFMAS system). Instead, we restrict the compositional space to a single parameter reflecting the degree of depletion of the mantle (Mg#). We then explore the broad range of compositions given by the xenoliths carried by volcanic rocks in the study area and the surroundings (Table 1). These simplifications enable us to solve the forward problem numerically with a high resolution (the vertical grid step in our computational domain is 500 m, which requires ~ 800 nodes) and at a low computational cost.

[22] In many locations around the globe, these assumptions are likely to apply. Elsewhere, modeling with these assumptions could produce a first-order, reference structure that can be used in a further analysis, with the fixed parameters and relationships allowed to vary or targeting non-isostatic and non-steady state effects.

4. Inversion for Baikal–Central Mongolia’s Lithospheric Structure

4.1. Fixed Parameters

[23] We assume a four-layered crust characterized, in part, by fixed parameters given in Table 2. V_P in the crust is constrained independently by previous

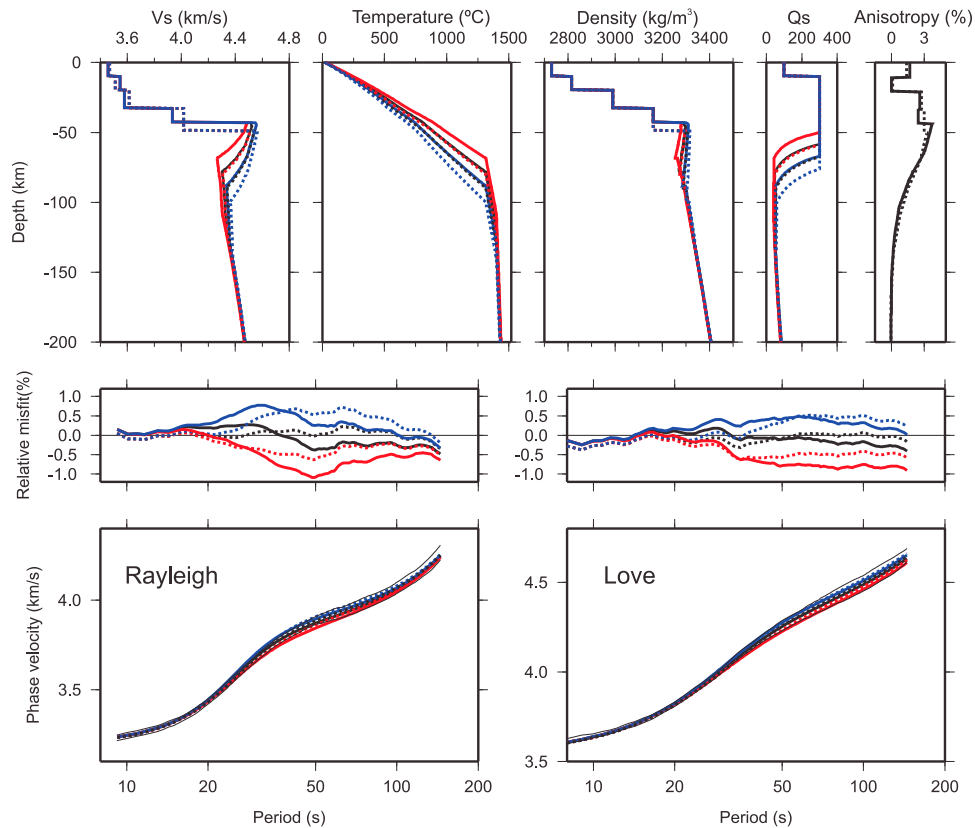


Figure 2. Example models of the lithosphere from the grid search inversion. (top) Isotropic-average anelastic S -wave speed, temperature, density, attenuation and radial anisotropy ($V_{SH} > V_{SV}$). Synthetic (bottom left) Rayleigh-wave and (bottom right) Love-wave phase-velocity curves, plotted together with the measured phase-velocity curves plus/minus one standard deviation (thin black lines). (Formal standard errors of the measurements, which were averaged from many hundreds of one-event measurements, are much smaller, comparable to the line thicknesses on this figure, and are not plotted.) (middle) Misfit between the synthetic and measured phase velocities. Same line colors and textures correspond to the same models throughout. Solid and dotted lines correspond to the Moho depths of 43 km and 49 km, respectively. Black lines: best fitting models with an LAB depth of 80 km (43 km Moho depth) and 90 km (49 km Moho depth). Models with thicker (blue lines) or thinner (red lines) lithosphere show larger misfits.

seismic refraction studies [Nielsen and Thybo, 2009]. The average measured thermal conductivity of the crystalline basement in Baikal and central Mongolia is about 2.5 W/m K, with the exception of the volumetrically low Cenozoic basalts for which the thermal conductivity is 1.5–1.7 W/m K [Lysak, 1995, and references therein]. The radiogenic heat production, as estimated from the abundances of U, Th and K, shows more scatter, and ranges from 0.5 to 2 $\mu\text{W}/\text{m}^3$ in the uppermost crust [Dorofeeva and Lysak, 1989; Lysak, 1995]. Since there are no direct measurements of heat production and thermal conductivity values at deeper levels, we assume standard values from the literature [Hasterok and Chapman, 2011; Jaupart and Mareschal, 2003; Rudnick and Fountain, 1995; Rudnick et al., 1998; Vilà et al., 2010] (Table 2). For the sub-lithospheric

mantle, a standard primitive upper mantle composition ($\text{Mg}\# = 89.3$) is assumed (Table 1).

4.2. Results

[24] Figure 2 displays 6 selected models tested in the course of the inversion and their fit to the measured phase-velocity curves. We inverted the dispersion curves only in the period ranges that are most sensitive to the lithosphere. We thus disregarded the very-long-period portions of the phase-velocity curves measured by Lebedev et al. [2006], sensitive to the lower half of the upper mantle (see auxiliary material). The models shown in Figure 2 include those with Moho depths in the upper and lower bounds of the best fitting range derived in our inversion (43 to 49 km below the mean sea level), LAB depths of 70, 80, 90 and 100 km and the

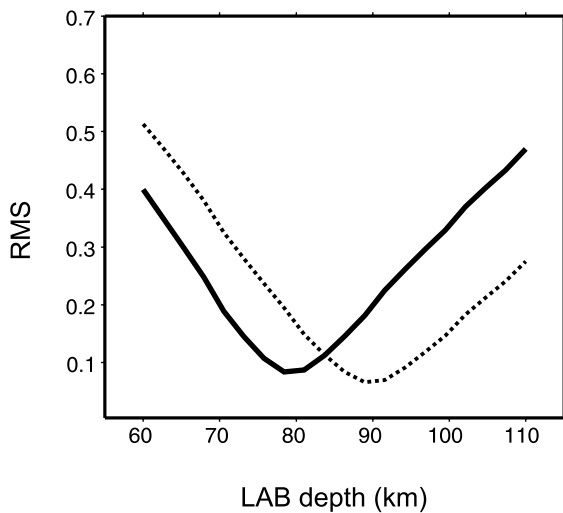


Figure 3. RMS of misfits between synthetic and measured phase velocities (including both Rayleigh and Love waves) as function of the LAB depth for the best fitting models shown in Figure 2. Solid and dotted lines correspond to the Moho depths of 43 km and 49 km, respectively.

lithospheric mantle composition characterized by $Mg\# = 89.7$ (see Table 1). The grid step for the LAB depth in the search was 2.5 km. All the depths are relative to the mean sea level. The best fitting models with 43-km and 49-km deep Mohos have LABs at 80 and 90 km, respectively (black lines). “Warmer” (with a thinner lithosphere) and “colder” (thicker lithosphere) models, shown with red and blue lines, respectively, provide substantially worse fits to the measured phase-velocity curves, as shown by the higher corresponding RMS values (Figure 3).

[25] Our best fitting models were computed assuming a mantle potential temperature, T_p , of 1340–1350°C. This value falls well within the expected range of values for ambient mantle, i.e., $T_p = 1280$ –1400°C, excluding mantle plumes or hot spots [Herzberg *et al.*, 2007]. In Figure 4 we explore the effect of varying T_p within the range 1280–1400°C for one of our preferred models, assuming a fixed temperature at the bottom of the model (T_{bot}). Given our parameterization, varying the temperature at the bottom of the buffer (i.e., T_{buffer} , see section 3.2 and equation (1)) implies changing T_p . The variations in T_p have a large effect on long-period Rayleigh waves sensitive to the deep upper mantle (not our focus in this paper) but translate into only moderate changes in the best fitting LAB depths (± 5 km) (Figure 4). We note that the model with the coldest sub-lithospheric mantle shown in Figure 4 ($T_p = 1280^\circ\text{C}$) is equivalent to a model without a

superadiabatic buffer zone beneath the lithosphere, given our parameterization.

[26] Figure 5 illustrates the relationships between the modeled topography and surface heat flow, lithospheric and crustal thicknesses, mantle composition and the average crustal density. The predicted isostatic topography depends on the integrated density of the column, i.e., on the crustal density and the temperature and composition distribution within the mantle. Models that fit both the surface-wave data and topography require a relatively high average crustal density of 2960–2980 kg/m³ (Table 3). A change of 6 km in the Moho depth or of 10 km in the LAB depth results in a change in the calculated topography of up to 300 m, a value close to the standard deviation of the average measured topography along the TLY-ULN corridor (the standard deviation can be considered a conservative estimate of the uncertainty in the elevation data modeling (Figure 1)). Therefore, such variations in the crustal and lithospheric thicknesses (i.e., 6 km and 10 km respectively) give rough estimates of the resolution of the Moho and LAB depths provided by the local isostasy modeling. Mantle composition has only a moderate effect on seismic velocities. In Figure 5 (bottom right) we show models with a Moho depth of 46 km that fit surface-wave data for a range of LAB depths and lithospheric mantle compositions from the fertile, sub-lithospheric composition to the highly depleted composition derived from xenoliths in the Siberian Craton (Table 1). The change in seismic velocities from the most fertile (slow) to the most depleted (fast) composition can be compensated by modifying the LAB depth (i.e., the corresponding kink in the geotherm) by only 4 km.

[27] Mantle composition has a much larger effect on the calculated topography through its effect on the lithospheric density. Models with compositions ranging from fertile sub-lithospheric ($Mg\# = 89.3$) to moderately depleted (i.e., Dariganga xenoliths, $Mg\# = 90.2$) fit the average topography of 1140 m within its standard deviation (i.e., <300 m). However, models with lithospheric composition given by the depleted Siberian Craton xenoliths (i.e., $Mg\# > 90.8$, see Table 1) predict high topography values that are clearly out of the range (>1400 m).

[28] The local isostatic balance is the result of the trade-off between the effects of temperature (mantle density increasing with decreasing temperature) and composition (mantle density decreasing with increasing depletion). The lithospheric mantle is usually more depleted than the underlying sub-lithospheric mantle and, therefore, an increase in

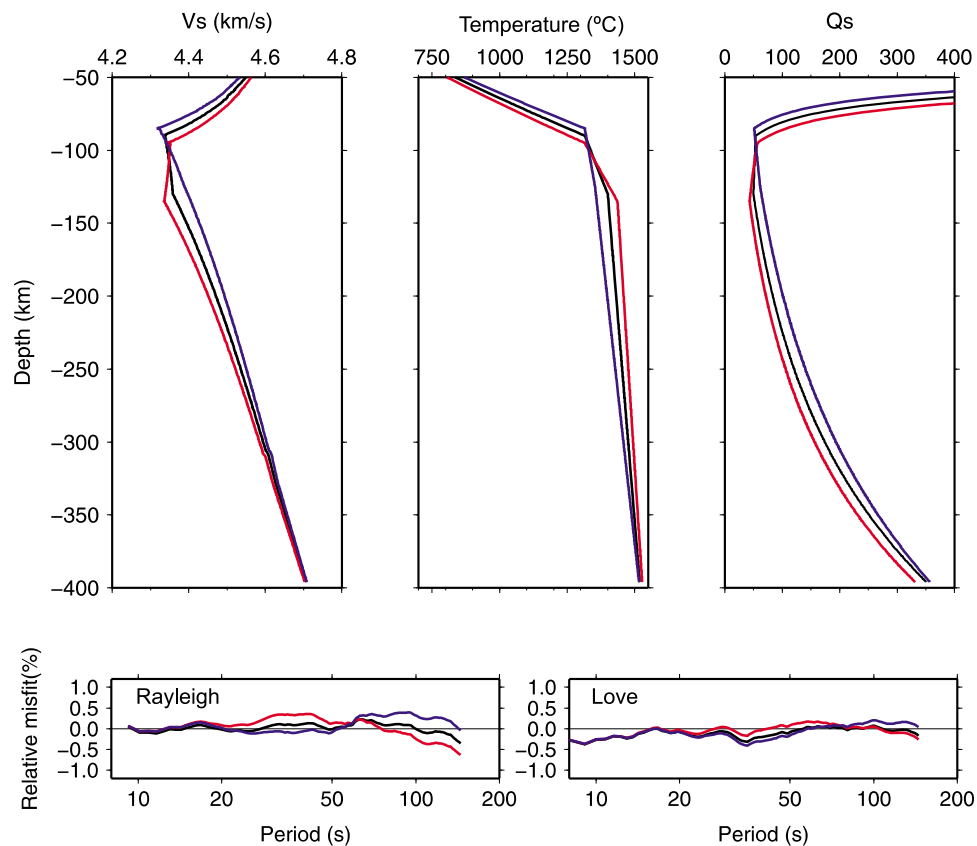


Figure 4. The effect of varying the potential temperature, T_p , in the sub-lithospheric mantle. Blue, black and red lines refer to T_p values of 1280°C, 1350°C and 1400°C respectively. (top left) Isotropic-average anelastic V_s profiles computed with the corresponding Q_s depicted in the top right plot. (top middle) Temperature profiles. (top right) Shear wave quality factors (Q_s) for the different geotherms shown in Figure 4 (top middle). Misfit between the synthetic and measured phase velocities for (bottom left) Rayleigh and (bottom right) Love waves for the different (anelastic) V_s profiles (Figure 4, top left). Same line colors correspond to the same models throughout. The Moho depth is 49 km in all the models. The LAB depth is 85 km, 90 km and 95 km for the models depicted with blue, black and red lines respectively.

the LAB depth (i.e., the thickness of the conductive mantle domain) has a twofold effect: i) replacing fertile sub-lithospheric material by more depleted (less dense) lithospheric mantle, and ii) making the lithospheric mantle colder and, hence, denser. For fertile to moderately depleted lithospheric compositions, the effect of ii) is much stronger than that of i): the thicker the lithosphere, the higher the average lithospheric mantle density, and the lower the calculated topography (Figure 6). Only for strongly depleted, cratonic compositions ($Mg\# > 92$) and large lithospheric thicknesses, the competing effects of i) and ii) can cancel each other out (e.g., $Mg\# = 92.3$ in Figure 6).

[29] The predicted surface heat flow is relatively insensitive to moderate crustal thickness variations ($<1 \text{ mW/m}^2$ change between the 43-km and 49-km Moho-depth end-members models) but varies

considerably with the lithospheric thickness. Our results indicate that LAB depths within a 70–100 km range would match the measured surface heat flow of 50–60 mW/m^2 (Figure 5).

[30] Our models show a monotonic decrease in shear velocities from the Moho to the bottom of the lithosphere. This is in contrast with many published models that show a shear-velocity increase with depth in the uppermost mantle [e.g., *Gaherty and Jordan, 1995; Fishwick and Reading, 2008; Lebedev et al., 2009*]. A plausible explanation for such increase is the spinel-garnet phase transition in the mantle [*Hales, 1969*]. Beneath cratons, the transformation can shift to greater depths and spread over broad depth intervals, due to the relatively Cr-rich compositions ($\text{Cr}/(\text{Cr} + \text{Al}) > 0.2$) [*Klemme, 2004; Lebedev et al., 2009*]. In this study no seismic-velocity increase with depth is seen in the

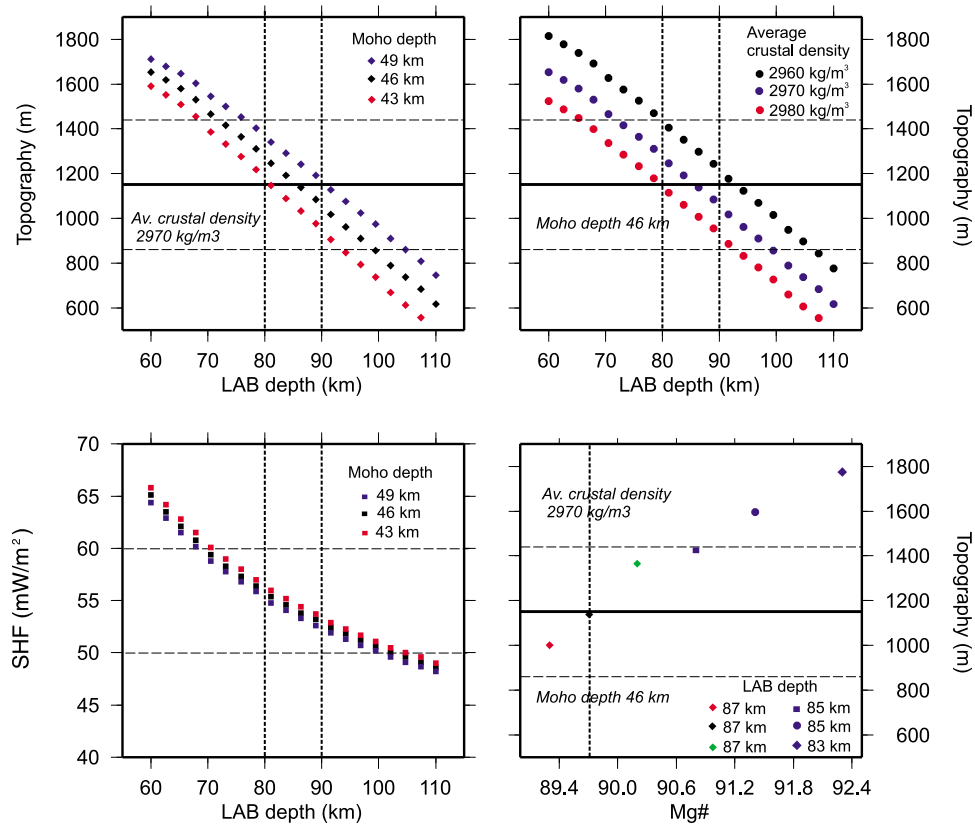


Figure 5. Relationships between LAB depth, crustal thickness and density, and calculated topography and surface heat flow (SHF). (top left) Calculated topography as a function of LAB depth. Red, black and blue diamonds correspond to models with Moho depths of 43, 46 and 49 km, respectively, all with an average crustal density of 2970 kg/m^3 . (bottom left) Calculated SHF as a function of LAB depth. Red, black and blue squares: models with the Moho depths of 43, 46 and 49 km respectively. Horizontal dashed lines delimit the range of the SHF measurements in the region. (top right) Calculated topography as a function of the LAB depth. Red, blue and black circles: models with average crustal densities of 2980 kg/m^3 , 2970 kg/m^3 , and 2960 kg/m^3 , respectively, all with the Moho depth of 46 km. (bottom right) Calculated topography as a function of the lithospheric mantle composition, assuming a Moho depth of 46 km and an average crustal density of 2970 kg/m^3 . The LAB depth is adjusted slightly in each case, so as to fit the surface-wave data (see legend in the bottom right corner of the frame). Red, black and green diamonds correspond to sub-lithospheric (fertile), Mongolian average and Dariganga (slightly depleted) compositions. Blue squares, circles and diamonds correspond to depleted Siberian Craton compositions (Table 1). The thick black horizontal lines show the average observed topography between TLY and ULN (Figure 1), with the standard deviation shown by thin, dashed lines. The vertical lines show the best fitting model parameters (i.e., LAB depth and Mg#).

uppermost mantle, neither in the petro-physical models, nor in the purely seismic inversions (Section 4.5). Given that the thermodynamic database and solid solution models used in this study do not include Cr (section 3.2), the sp-gnt phase transition occurs at a specific depth due to its univariant nature (near the depth of the Moho in our case). The addition of small amounts of Cr (e.g., Table 1) would make the transition divariant but the sp-gnt stability field would still remain relatively narrow given the fertile lithospheric mantle composition in our preferred models ($\text{Mg\#} < 90.2$) [Ayarza *et al.*, 2010].

Table 3. Densities and Layer Thicknesses in the Best Fitting Models

Layer	Density (kg/m^3)	Depth of Base (km)
Uppermost crust	2730–2750	10 ^a
Mid-upper crust	2815–2835	20 ^a
Mid crust	3020–3050	33 ^a
Lower crust	3160–3200	43–49
Lithosphere mantle	composition 1 ^b	80–90
Sub-lithosphere	composition 2 ^b	400

^aThe thickness of these layers is fixed in the inversions (see Table 2).

^bMantle densities are calculated as a function of temperature, pressure and bulk composition see the text for further details. Mantle compositions 1 and 2 are shown in Table 1.

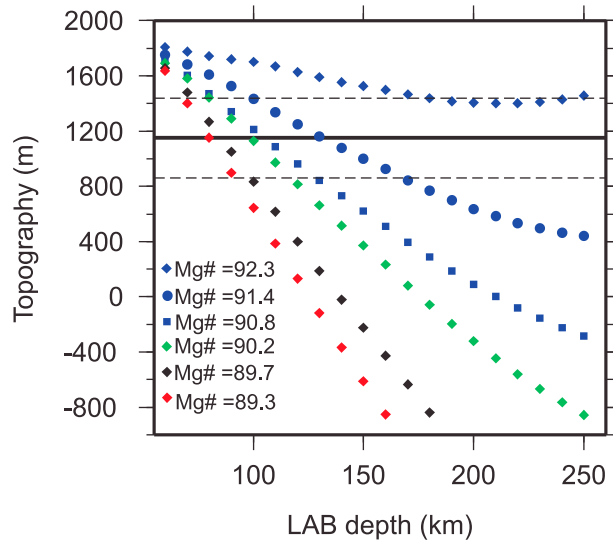


Figure 6. Calculated topography as a function of the LAB depth for the mantle compositions listed in Table 1. Red, black and green diamonds correspond to sub-lithospheric (fertile), Mongolian average (slightly depleted) and Dariganga (slightly depleted) compositions respectively. Blue squares, circles and diamonds correspond to depleted Siberian Craton compositions (Table 1).

4.3. Importance of Radial Anisotropy

[31] Surface-wave data require radial anisotropy of ($V_{SH} > V_{SV}$) of a few percent in the crust and lithospheric mantle of central Mongolia; this is similar in magnitude to the radial anisotropy in global-average models [Dziewonski and Anderson, 1981]. In Figure 7, we plot the anisotropy profiles associated with two of our best fitting models (solid and dotted black lines as in Figure 2) together with other anisotropy profiles (gray lines) that fit the data equally well. The profiles used for our modeling (black lines) are smooth and conservative (no oscillatory variations of anisotropy with depth), with maximum anisotropy in the lower crust and lithospheric mantle of around 3%.

[32] Anisotropy has a strong effect on the inversions for lithospheric structure. It has long been known that neglecting radial anisotropy can bias estimates of the lithospheric thickness [e.g., Gung et al., 2003]. Here, we perform a series of tests in order to evaluate the effect of anisotropy specifically on the lithospheric thickness given by our geophysical-petrological inversion. We find that, given radial anisotropy beneath central Mongolia (Figure 7), the inversion of Rayleigh-wave data alone under the assumption of no anisotropy would result in a 10–15 km error in the LAB depth (see auxiliary material for further details).

4.4. Anelastic Attenuation

[33] Much of the attenuation observed in seismic waves is caused by the thermally activated viscoelastic relaxation of the mineral aggregates within the Earth. The importance of attenuation effects in inversions of seismic data for the thermal and compositional structure of the upper mantle is well known [e.g., Afonso et al., 2010; Cammarano and Romanowicz, 2008; Goes et al., 2000; Sobolev et al., 1996]. Our understanding of viscoelastic relaxation at seismic frequencies ($10\text{--}10^{-4}$ Hz) in upper mantle mineral aggregates or analogues, and the relation between attenuation and grain size,

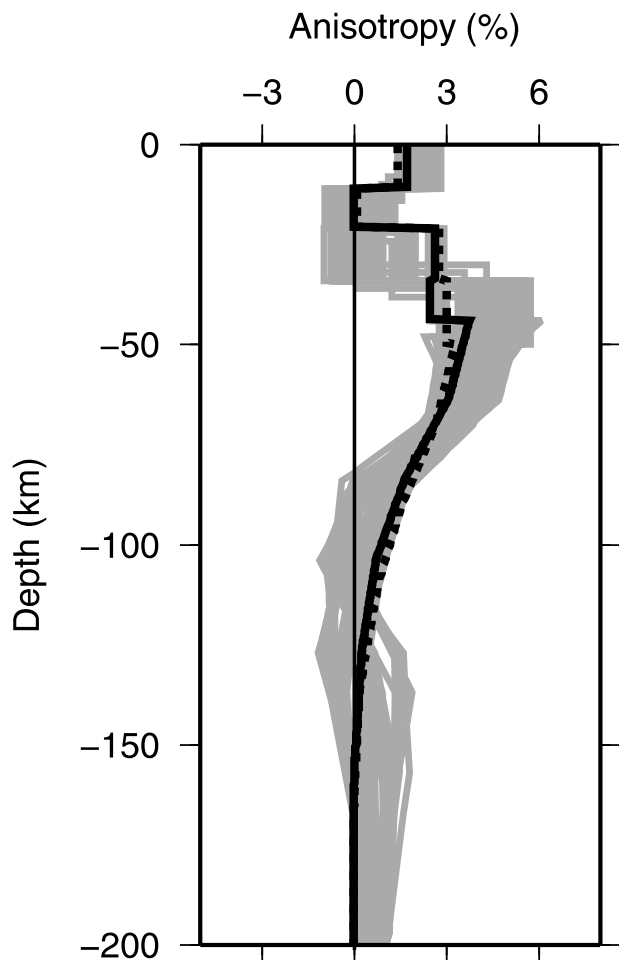


Figure 7. Radial anisotropy profiles associated with our best fitting models (solid and dotted black lines in Figure 2) together with other anisotropy profiles (gray lines) that fit the surface-wave data. (Paired with appropriate isotropic shear-speed profiles, these anisotropy profiles, each computed in a nonlinear gradient-search inversion, produce synthetic Rayleigh and Love-wave dispersion curves that differ from each other by less than 0.2% at any period up to 250 s.)

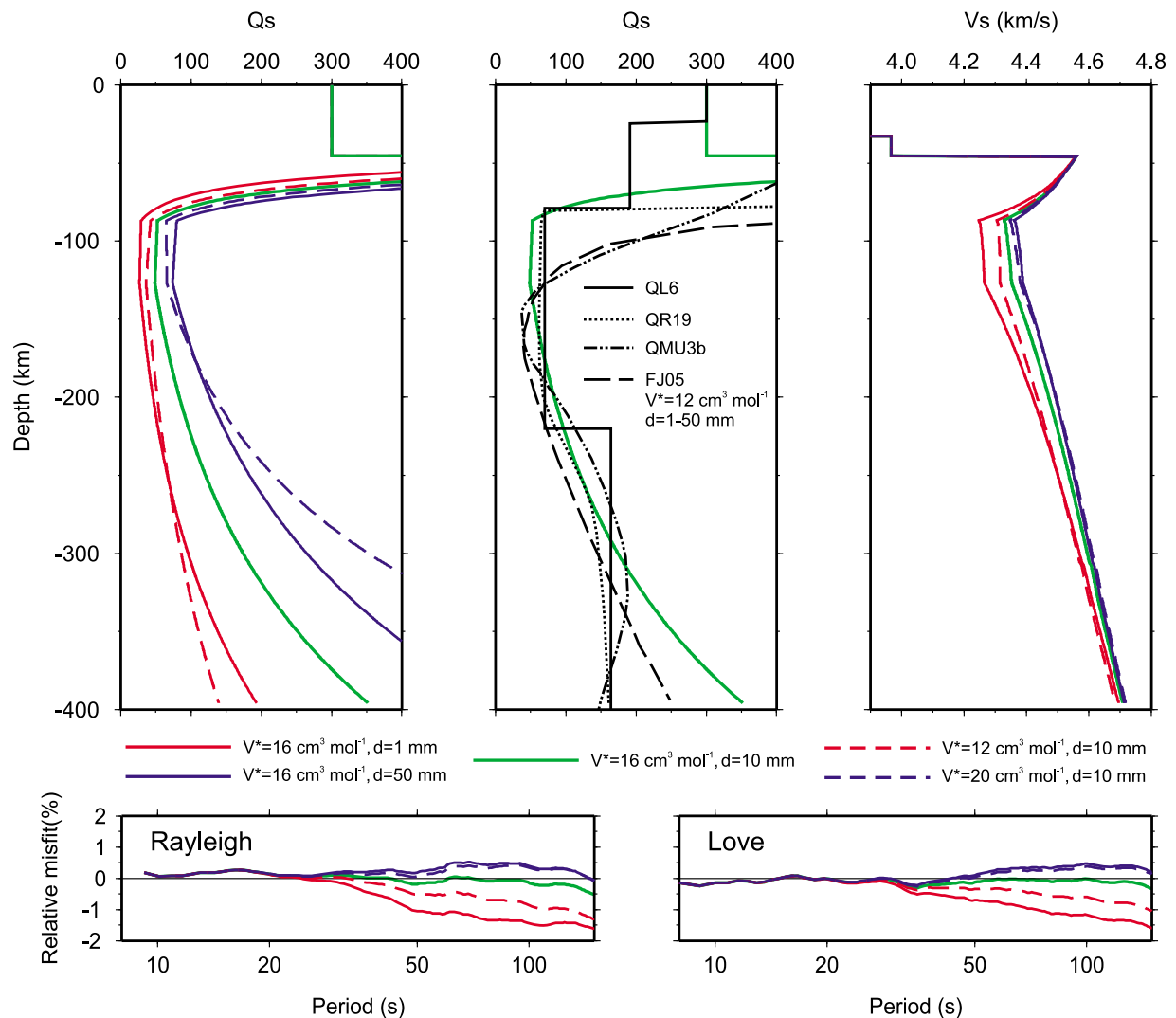


Figure 8. The effect of attenuation, grain size and activation volume in the mantle. (top left) Shear wave quality factors (Q_s) for different activation volumes (V^*) and grain sizes (d), all with the Moho and LAB depths of 46 km and 87 km, respectively. (top middle) Our preferred Q_s model (green line) and the radial seismic models QL6 [Durek and Ekström, 1996], QR19 [Romanowicz, 1995], QMU3b [Selby and Woodhouse, 2002]. FJ05 is based on the experimental results of Faul and Jackson [2005] for a gradually increasing d from 1 mm to 50 mm with increasing depth below 165 km, and $V^* = 12 \text{ cm}^3 \text{ mol}^{-1}$. (top right) Anelastic V_s profiles computed with the different Q_s models depicted in the top left plot. Misfit between the synthetic and measured phase velocities for (bottom left) Rayleigh and (bottom right) Love waves for the different anelastic V_s profiles (Figure 8, top right). Same line colors and textures correspond to the same models throughout.

have improved considerably in recent years thanks to new laboratory studies [e.g., Jackson and Faul, 2010; McCarthy et al., 2011].

[34] In this work we compute pressure- and temperature-dependent shear wave quality factors, Q_s , based on mineral physics relationships for dry and melt-free polycrystalline olivine (equation (2)). The main parameters in equation (2) are the grain size, d , and the activation volume, V^* . We chose parameter

values ($d = 10 \text{ mm}$ and $V^* = 16 \text{ cm}^3 \text{ mol}^{-1}$) that predict attenuation profiles compatible with seismologically measured Q_s models, and explore the effect of variations in d and V^* within the experimental ranges, extrapolated to upper mantle conditions (Figure 8). Grain size in mantle rocks is controlled by the trade-off between crystal growth (which increases d) and recrystallization (which decreases d), and may vary over a broad range in the upper mantle (1 mm–50 mm). The activation volume

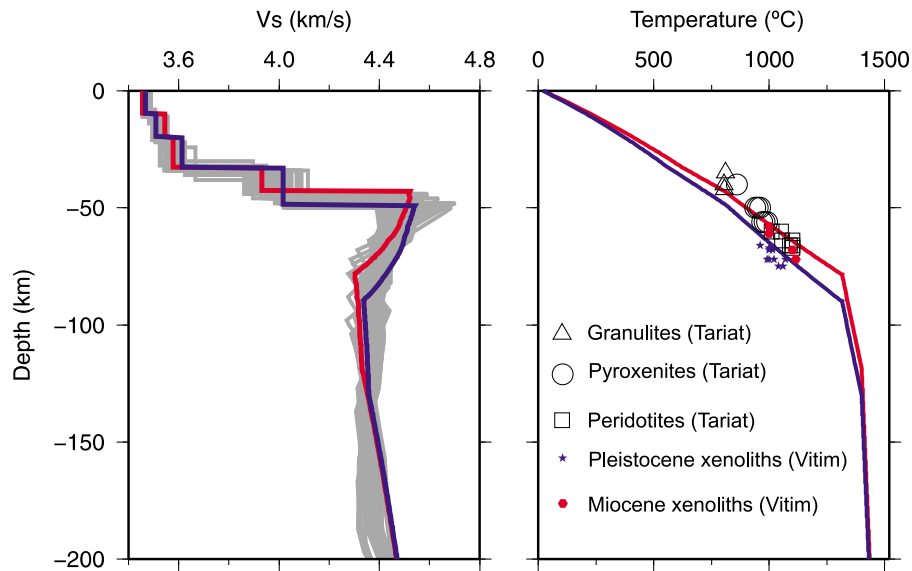


Figure 9. Purely seismic and petro-physically derived models of Baikal–central Mongolia lithosphere. Red and blue lines: petro-physical models with 43 and 49 km Moho depths and 80 and 90 km LAB depths, respectively; the models delimit the range of best fitting Moho and LAB depths. (left) Isotropic-average, S -wave speed profiles obtained by seismic (gray lines) and integrated petrological-geophysical (red and blue) inversions. (right) Calculated geotherms for our best fitting models. Thermo-barometric data from crustal and mantle xenoliths in Tariat and Vitim (Figure 1) are from *Ionov* [2002, and references therein].

accounts for the pressure effect on Q_s . Here, we explore a range of plausible values ($V^* = 12 \text{ cm}^3 \text{ mol}^{-1}$ to $20 \text{ cm}^3 \text{ mol}^{-1}$), suggested by experimental results [e.g., *Faul and Jackson, 2005*].

[35] Grain size or activation volume at the lower bounds of the ranges (solid and dashed red lines in Figure 8) predict too low Q_s and too low V_s values in the lower lithosphere and uppermost sub-lithospheric mantle; the large, negative phase-velocity residuals and the change of phase-velocity-curve slopes due to the high attenuation would be difficult to reconcile with the observed phase velocities. This indicates that the very low Q_s values are unlikely to occur in the mantle beneath central Mongolia. Very large grain sizes and activation volumes, in contrast, decrease attenuation (solid and dashed blue lines in Figure 8) and translate into only moderately faster V_s than in our preferred model (green line in Figure 8), giving rise to relatively small, positive residuals in the synthetic phase velocities. These values could be reconciled with seismic data easily, through a small increase in temperature (decrease in thickness) of the lithosphere in the models.

4.5. Lithospheric Structure

[36] In Figure 9 (left) we compare the V_S profiles of the “coldest” (blue) and “hottest” (red) of the

best fitting models given by our geophysical-petrological inversion with a range of profiles (gray) obtained by inverting seismic data only (inversions of phase velocities directly for V_S profiles [e.g., *Lebedev et al., 2006*]). Synthetic Love and Rayleigh phase velocities computed for the different gray profiles fit the data almost equally well, differing from each other by less than 0.2% at any period up to 250 s. The geophysical-petrological inversion strongly reduces the non-uniqueness of the lithospheric models that fit the phase-velocity data, largely through its implicit physical constraints on the V_s gradients within the lithospheric and sub-lithospheric mantle.

[37] The sub-lithospheric structure beneath central Mongolia shows moderate seismic-velocity anomalies with respect to global reference models, according to published seismic tomography [e.g., *Koulakov and Bushenkova, 2010; Lebedev and van der Hilst, 2008*]. Low-velocity anomalies localized beneath the Baikal Rift Zone have been interpreted as evidence for a thermal upwelling [e.g., *Zhao et al., 2006*]. A large-scale thermal upwelling, however, would result in an anomalously hot uppermost asthenosphere beneath central Mongolia, just south of Baikal. The consistency of seismic, topography, and surface heat flow data with the global-average sub-lithospheric geotherm ($T_p = 1340\text{--}1350^\circ\text{C}$), as shown by our inversions, does not indicate any

significant thermal anomaly just below the LAB (Figure 4).

[38] The 80–90 km LAB depth given by our best fitting models is consistent with the 80–100 km values across Mongolia on the LAB-depth map of *Rychert and Shearer* [2009], derived from teleseismic receiver functions. Our models reproduce seismic velocities near the LAB in detail and show a structure (changes of slope in the V_S and V_P profiles at the LAB) that could give rise to detectable P - s and S - p conversions. Reconciling surface-wave and receiver-function data (future work) should yield new insight into the nature of the LAB.

[39] Xenolith data offer complementary constraints on the lithospheric paleogeotherm, seismic anisotropy and composition. Thermobarometry data from garnet-bearing xenolith suites from Tariat and Vitim regions (Figure 1) are also plotted in Figure 9. Pressure-Temperature estimates were obtained by *Ionov* [2002] using the Ca-in-opx thermometer of *Brey and Köhler* [1990] combined with the barometer of *Nickel and Green* [1985]. Projections of the lowest temperatures derived from xenoliths in the spinel stability field in Tariat are also shown. The P , T estimates from xenoliths entrained in Miocene and Pleistocene volcanic rocks provide an independent benchmark and show a very good agreement with the present-day geotherms determined by our modeling. Optical studies of mantle xenoliths from Vitim made by *Kern et al.* [1996] suggest P - and S -wave anisotropy of 4.0–6.5%, qualitatively consistent with the amplitude of radial anisotropy constrained by surface-wave data (Figure 7). The ratio of the P - and S -wave velocities, V_P/V_S , is highly sensitive to the mafic/felsic nature of the crust, and relatively insensitive to temperature variations [e.g., *Christensen*, 1996]. Together with density, V_P/V_S is a good proxy for the crustal composition. We can estimate a value of $V_P/V_S = 1.82$ – 1.83 and a density of 3160–3200 kg/m³ for the lower crust in Central Mongolia, using our models for V_S and density and published values for V_P (Tables 2 and 3 and Figures 2 and 5). According to laboratory measurements, these values fall within the range characteristic of mafic garnet granulite rock type [*Christensen*, 1996]. This composition is also confirmed by some of the xenoliths erupted in Tariat (Figure 1), sampling the lower crust close to the Moho and exhibiting pyroxene and garnet granulite facies [*Stosch et al.*, 1995].

[40] The observed topography (1.2 km on average along the TLY-ULN corridor) can be fully accounted

for by local isostasy, without any dynamic component due to a thermal upwelling. If a large scale mantle upwelling related to the Baikal Rift was present, causing positive dynamic topography, then the topography predicted by our models (assuming local isostasy) should be below the observed topography. According to our calculations, dynamic topography could be present if: i) the average crustal density was >2980 kg/m³, or ii) the LAB was deeper than around 100 km (i.e., the lithospheric mantle density was increased) (Figure 5). The first scenario implies an unrealistically dense crust, much denser than the mafic, already dense lower crust required by our data (Figure 5) (a layer of mafic underplated cumulates or mafic granulites in the uppermost mantle has previously been proposed for the elevated Hangai Dome area (Tariat, see Figure 1), west of our corridor [*Petit et al.*, 2002].) In the second, the Mongolian lithosphere would be too cold, with predicted values for phase velocities too large (Figures 2 and 3), and the calculated surface heat flow would be lower than the measured values (Figure 5).

[41] Uncertainties in the mantle composition also cannot conceal any significant dynamic topography: replacing our preferred lithospheric composition ($Mg\# = 89.7$) by that of the fertile sub-lithospheric mantle ($Mg\# = 89.3$) would decrease the predicted topography by very little (<200 m), whereas more depleted lithospheric mantle would translate into higher surface elevation in isostatic equilibrium (even less consistent with any positive dynamic topography (Figure 5)).

[42] The moderate thickness of the lithosphere (80–90 km thick) constrained by our inversions and the absence of a thermal anomaly in the uppermost sub-lithospheric mantle are consistent with the measured regional surface heat flow, moderate in comparison with that in other active rifting areas in the world, and are not indicative of any recent, active mantle upwelling. Mantle xenoliths do not show any evidence of recent melting or abnormal deformation within the lithospheric mantle down to 70 km depth, in agreement with the lithosphere being 80–90 km thick, as determined in this study. If there was any significant melt-metasomatism or heating of the lithospheric mantle, it could only occur at depths >70 km [*Barry et al.*, 2003; *Ionov*, 2002]. The lithospheric and sub-lithospheric structure beneath central Mongolia does not indicate substantial thermal anomalies and is consistent with passive rifting in the Baikal Rift Zone, driven by far field tectonic forces [e.g., *Molnar and Tapponnier*,

1975; *Petit et al.*, 1997; *Petit and Déverchère*, 2006; *Tiberi et al.*, 2003].

5. Conclusions

[43] Thanks to the recent progress in petro-physical modeling and in the accuracy of seismic measurements, subtle variations in surface-wave dispersion can now be related to fine-scale structure of the lithosphere. In this study we tested a proof-of-concept inversion of fundamental-mode, Rayleigh- and Love-wave phase-velocity curves and topography for lithospheric temperature and composition. The grid-search inversion used a self-consistent thermodynamic framework, with all relevant mantle properties computed as a function of temperature, pressure and composition. Surface heat flow, seismic-refraction-derived crustal models, and xenolith data provided additional constraints and validation of the modeling. Models with conductive lithospheric geotherms, computed using a P-T-dependent thermal conductivity, are consistent with surface-wave data from central Mongolia. The assumption of a steady state geotherm in the lithospheric mantle should be sufficiently accurate to determine the lithospheric structure with useful accuracy in many locations; in other locations, it can provide meaningful reference models to investigate non steady state effects.

[44] Quantifying the inter-relationships and trade-offs between the LAB depth, crustal thickness and density, topography, surface heat flow, and the depletion of the lithospheric mantle (expressed as Mg#), we show that surface-wave and topography data can constrain robust, high-resolution lithospheric models. Seismic attenuation must be modeled accurately; our results confirm that published ranges of the grain-size and activation-volume values, on which attenuation depends, are consistent with seismic data. Radial anisotropy also needs to be taken into account; neglecting anisotropy can result in errors in the LAB depth exceeding 10 km.

[45] The *S*-wave velocity mantle profiles derived from our petro-physical inversion are remarkably consistent in their basic shape with profiles that result from purely seismic inversions of surface-wave phase velocities. This consistency is significant because the forward problems and the set-ups and parameterizations of the two inversion schemes are fundamentally different; it validates our integrated inversion. The clear advantage of the petro-physical inversion is that it strongly reduces the non-uniqueness of the lithospheric models that result from seismic inversions

(Figure 9), through the addition of complementary geophysical and petrological information. Another important advantage is that the density at depth can be constrained by the inversion if surface topography is included as data.

[46] Our results show that the depth of the LAB in Baikal–central Mongolia, defined as the bottom of the thermally conductive mantle layer, is 80–90 km. This is within the range of published receiver function results; importantly, our models also reveal a second-order discontinuity (jump in the radial wave speed derivative) at the (“thermal”) LAB that can give rise to detectable *P*-*s* and *S*-*p* conversions. The crustal thickness is 44–50 km and the predicted surface heat flow is 53–55 mW/m². Pressure and temperature estimates from mantle xenoliths in central Mongolia fit the geotherm defined by our preferred models, providing further validation of the method. The mid-lower crust in Central Mongolia, according to our inversion, is relatively dense (3160–3200 kg/m³) and mafic in nature (mafic garnet granulite). This is consistent with lower-crust xenoliths data from Mongolia (Tariat).

[47] The average topography observed in central Mongolia can be fully explained by local isostasy. A substantial dynamic component in the topography, as would be required by a large scale mantle upwelling, can be ruled out by the surface-wave and heat flow data. The thermal structure of the lithosphere and asthenosphere constrained by our inversion does not show any evidence for abnormally high temperature (i.e., $T_p > 1400^\circ\text{C}$) that could be associated with a presently active hot mantle plume and is consistent, instead, with a passive rifting process in the Baikal Rift Zone.

Acknowledgments

[48] We thank Derek Schutt, Lapo Boschi, Associate Editor James Gaherty and Senior Editor Thorsten Becker for insightful comments that helped us to improve the manuscript. Figures were generated with Generic Mapping Tools [*Wessel and Smith*, 1995]. JF was supported by an IRCSET grant to AGJ for the *TopoMed* project within the TOPO-EUROPE EUROCORES and the JAE-Doc Programme from Spanish CSIC, co-funded by FSE. This work was supported (SL and MRA) by Science Foundation Ireland (grant 08/RFP/GEO1704). JCA acknowledges support from the Australian Research Council through a Discovery Grant (DP120102372). This is contribution 192 from the ARC Centre of Excellence for Core to Crust Fluid Systems (<http://www.ccfcs.mq.edu.au>) and 835 in the GEMOC Key Centre (<http://www.gemoc.mq.edu.au>).

References

- Afonso, J. C., and S. Zlotnik (2011), The subductability of the continental lithosphere: The before and after story, in *Arc-Continent Collision*, edited by D. Brown and P. D. Ryan, pp. 53–86, Springer, Berlin, doi:10.1007/978-3-540-88558-0_3.
- Afonso, J. C., G. Ranalli, and M. Fernández (2005), Thermal expansivity and elastic properties of the lithospheric mantle: Results from mineral physics of composites, *Phys. Earth Planet. Inter.*, *149*(3–4), 279–306, doi:10.1016/j.pepi.2004.10.003.
- Afonso, J. C., M. Fernández, G. Ranalli, W. L. Griffin, and J. A. D. Connolly (2008), Integrated geophysical-petrological modeling of the lithosphere and sublithospheric upper mantle: Methodology and applications, *Geochem. Geophys. Geosyst.*, *9*, Q05008, doi:10.1029/2007GC001834.
- Afonso, J. C., G. Ranalli, M. Fernández, W. L. Griffin, S. Y. O'Reilly, and U. Faul (2010), On the Vp/Vs–Mg# correlation in mantle peridotites: Implications for the identification of thermal and compositional anomalies in the upper mantle, *Earth Planet. Sci. Lett.*, *289*, 606–618, doi:10.1016/j.epsl.2009.12.005.
- Anderson, D. L., and C. Sammis (1970), Partial melting in the upper mantle, *Phys. Earth Planet. Inter.*, *3*, 41–50, doi:10.1016/0031-9201(70)90042-7.
- Ayarza, P., I. Palomeras, R. Carbonell, J. C. Afonso, and F. Simancas (2010), A wide-angle upper mantle reflector in SW Iberia: Some constraints on its nature, *Phys. Earth Planet. Inter.*, *181*(3–4), 88–102, doi:10.1016/j.pepi.2010.05.004.
- Ballmer, M. D., G. Ito, J. van Hunen, and P. J. Tackley (2011), Spatial and temporal variability in Hawaiian hotspot volcanism induced by small-scale convection, *Nat. Geosci.*, *4*, 457–460, doi:10.1038/ngeo1187.
- Barry, T. L., A. D. Saunders, P. D. Kempton, B. F. Windley, M. S. Pringle, D. Dorjnamjaa, and S. Saandar (2003), Petrogenesis of cenozoic basalts from Mongolia: Evidence for the role of asthenospheric versus metasomatized lithospheric mantle sources, *J. Petrol.*, *44*(1), 55–91, doi:10.1093/petrology/44.1.55.
- Bartzsch, S., S. Lebedev, and T. Meier (2011), Resolving the lithosphere-asthenosphere boundary with seismic Rayleigh waves, *Geophys. J. Int.*, *186*, 1152–1164, doi:10.1111/j.1365-246X.2011.05096.x.
- Boschi, L., C. Faccenna, and T. W. Becker (2010), Mantle structure and dynamic topography in the Mediterranean Basin, *Geophys. Res. Lett.*, *37*, L20303, doi:10.1029/2010GL045001.
- Boyd, F. R., N. P. Pokhilenko, D. G. Pearson, S. A. Mertzman, N. V. Sobolev, and L. W. Finger (1997), Composition of the Siberian cratonic mantle: Evidence from Udachnaya peridotite xenoliths, *Contrib. Mineral. Petrol.*, *128*, 228–246, doi:10.1007/s004100050305.
- Brey, G. P., and T. Köhler (1990), Geothermobarometry in four phase lherzolites II: New thermobarometers and practical assessment of using thermobarometers, *J. Petrol.*, *31*, 1353–1378.
- Brune, J. N., and J. Dorman (1963), Seismic waves and earth structure in the Canadian Shield, *Bull. Seismol. Soc. Am.*, *53*, 167–210.
- Burov, E. B., F. Houdry, M. Diament, and J. Déverchère (1994), A broken plate beneath the North Baikal Rift zone revealed by gravity modelling, *Geophys. Res. Lett.*, *21*, 129–132, doi:10.1029/93GL03078.
- Calais, E., M. Vergnolle, V. San'kov, A. Likhnev, A. Miroshnichenko, S. Amarjargal, and J. Déverchère (2003), GPS measurements of crustal deformation in the Baikal-Mongolia area (1994–2002), Implications for current kinematics of Asia, *J. Geophys. Res.*, *108*(B10), 2501, doi:10.1029/2002JB002373.
- Cammarano, F., and B. Romanowicz (2008), Radial profiles of seismic attenuation in the upper mantle based on physical models, *Geophys. J. Int.*, *175*, 116–134, doi:10.1111/j.1365-246X.2008.03863.x.
- Cammarano, F., S. Goes, P. Vacher, and D. Giardini (2003), Inferring upper mantle temperatures from seismic velocities, *Phys. Earth Planet. Inter.*, *138*, 197–222, doi:10.1016/S0031-9201(03)00156-0.
- Cammarano, F., B. Romanowicz, L. Stixrude, C. Lithgow-Bertelloni, and W. Xu (2009), Inferring the thermochemical structure of the upper mantle from seismic data, *Geophys. J. Int.*, *179*, 1169–1185, doi:10.1111/j.1365-246X.2009.04338.x.
- Chambers, K., J. H. Woodhouse, and A. Deuss (2005), Topography of the 410-km discontinuity from PP and SS precursors, *Earth Planet. Sci. Lett.*, *235*, 610–622, doi:10.1016/j.epsl.2005.05.014.
- Christensen, N. I. (1996), Poisson's ratio and crustal seismology, *J. Geophys. Res.*, *101*(B2), 3139–3156, doi:10.1029/95JB03446.
- Connolly, J. (2005), Computation of phase equilibria by linear programming: A tool for geodynamic modeling and its application to subduction zone decarbonation, *Earth Planet. Sci. Lett.*, *236*(1–2), 524–541, doi:10.1016/j.epsl.2005.04.033.
- Connolly, J., and D. Kerrick (2002), Metamorphic controls on seismic velocity of subducted oceanic crust at 100–250 km depth, *Earth Planet. Sci. Lett.*, *204*(1–2), 61–74, doi:10.1016/S0012-821X(02)00957-3.
- Deal, M. M., and G. Nolet (1996), Nullspace shuttles, *Geophys. J. Int.*, *124*(2), 372–380, doi:10.1111/j.1365-246X.1996.tb07027.x.
- Deschamps, F., J. Trampert, and R. Snieder (2002), Anomalies of temperature and iron in the uppermost mantle inferred from gravity data and tomographic models, *Phys. Earth Planet. Inter.*, *129*, 245–264, doi:10.1016/S0031-9201(01)00294-1.
- Deschamps, F., S. Lebedev, T. Meier, and J. Trampert (2008), Azimuthal anisotropy of Rayleigh-wave phase velocities in the east-central United States, *Geophys. J. Int.*, *173*, 827–843, doi:10.1111/j.1365-246X.2008.03751.x.
- Dorofeeva, R. P., and S. V. Lysak (1989), Geothermal profiles of the lithosphere in central Asia, *Tectonophysics*, *164*(2–4), 165–173, doi:10.1016/0040-1951(89)90010-3.
- Duffy, T., and D. Anderson (1989), Seismic velocities in mantle minerals and the mineralogy of the upper mantle, *J. Geophys. Res.*, *94*(B2), 1895–1912, doi:10.1029/JB094iB02p01895.
- Durek, J. J., and G. Ekström (1996), A radial model of anelasticity consistent with long-period surface-wave attenuation, *Bull. Seismol. Soc. Am.*, *86*, 144–158.
- Dziewonski, A. M., and D. L. Anderson (1981), Preliminary reference Earth model, *Phys. Earth Planet. Inter.*, *25*(4), 297–356, doi:10.1016/0031-9201(81)90046-7.
- Eaton, D. W., F. Darbyshire, R. L. Evans, H. Grutter, A. G. Jones, and X. H. Yuan (2009), The elusive lithosphere-asthenosphere boundary (LAB) beneath cratons, *Lithos*, *109*(1–2), 1–22.
- Endrun, B., S. Lebedev, T. Meier, C. Tirel, and W. Friederich (2011), Complex layered deformation within the Aegean



- crust and mantle revealed by seismic anisotropy, *Nat. Geosci.*, *4*, 203–207, doi:10.1038/ngeo1065.
- Faul, U. H., and I. Jackson (2005), The seismological signature of temperature and grain size variations in the upper mantle, *Earth Planet. Sci. Lett.*, *234*, 119–134, doi:10.1016/j.epsl.2005.02.008.
- Fischer, K. M., H. A. Ford, D. L. Abt, and C. A. Rychert (2010), The lithosphere-asthenosphere boundary, *Annu. Rev. Earth Planet. Sci.*, *38*, 551–575.
- Fishwick, S., and A. M. Reading (2008), Anomalous lithosphere beneath the Proterozoic of western and central Australia: A record of continental collision and intraplate deformation?, *Precambrian Res.*, *166*, 111–121, doi:10.1016/j.precamres.2007.04.026.
- Forte, A. M., and H. K. C. Perry (2000), Geodynamic evidence for a chemically depleted continental tectosphere, *Science*, *290*(5498), 1940–1944, doi:10.1126/science.290.5498.1940.
- Forte, A. M., S. Quéré, R. Moucha, N. A. Simmons, S. P. Grand, J. X. Mitrovica, and D. B. Rowley (2010), Joint seismic–geodynamic–mineral physical modelling of African geodynamics: A reconciliation of deep-mantle convection with surface geophysical constraints, *Earth Planet. Sci. Lett.*, *295*(3–4), 329–341, doi:10.1016/j.epsl.2010.03.017.
- Frost, D. J. (2003), The structure and sharpness of $(\text{Mg}, \text{Fe})_2\text{SiO}_4$ phase transformations in the transition zone, *Earth Planet. Sci. Lett.*, *216*, 313–328, doi:10.1016/S0012-821X(03)00533-8.
- Frost, D. J., and D. Dolejš (2007), Experimental determination of the effect of H_2O on the 410-km seismic discontinuity, *Earth Planet. Sci. Lett.*, *256*, 182–195, doi:10.1016/j.epsl.2007.01.023.
- Fullea, J., J. C. Afonso, J. A. D. Connolly, M. Fernández, D. García-Castellanos, and H. Zeyen (2009), LitMod3D: An interactive 3-D software to model the thermal, compositional, density, seismological, and rheological structure of the lithosphere and sublithospheric upper mantle, *Geochem. Geophys. Geosyst.*, *10*, Q08019, doi:10.1029/2009GC002391.
- Fullea, J., M. Fernández, J. C. Afonso, J. Verges, and H. Zeyen (2010), The structure and evolution of the lithosphere-asthenosphere boundary beneath the Atlantic-Mediterranean Transition Region, *Lithos*, *120*, 74–95, doi:10.1016/j.lithos.2010.03.003.
- Fullea, J., M. R. Müller, and A. G. Jones (2011), Electrical conductivity of continental lithospheric mantle from integrated geophysical and petrological modeling: Application to the Kaapvaal Craton and Rehoboth Terrane, southern Africa, *J. Geophys. Res.*, *116*, B10202, doi:10.1029/2011JB008544.
- Gaherty, J. B., and T. H. Jordan (1995), Lehmann discontinuity as the base of an anisotropic layer beneath continents, *Science*, *268*, 1468–1471, doi:10.1126/science.268.5216.1468.
- Gao, S. S., K. H. Liu, P. M. Davis, P. D. Slack, Y. A. Zorin, V. V. Mordvinova, and V. M. Kozhevnikov (2003), Evidence for small-scale mantle convection in the upper mantle beneath the Baikal rift zone, *J. Geophys. Res.*, *108*(B4), 2194, doi:10.1029/2002JB002039.
- Gao, S. S., K. H. Liu, and C. Chen (2004), Significant crustal thinning beneath the Baikal Rift zone: New constraints from receiver function analysis, *Geophys. Res. Lett.*, *31*, L20610, doi:10.1029/2004GL020813.
- Goes, S., R. Govers, and P. Vacher (2000), Shallow mantle temperatures under Europe from P and S wave tomography, *J. Geophys. Res.*, *105*, 11,153–11,169, doi:10.1029/1999JB000300.
- Gung, Y., M. Panning, and B. Romanowicz (2003), Global anisotropy and the thickness of continents, *Nature*, *422*, 707–711, doi:10.1038/nature01559.
- Hales, A. L. (1969), A seismic discontinuity in the lithosphere, *Earth Planet. Sci. Lett.*, *7*, 44–46, doi:10.1016/0012-821X(69)90009-0.
- Hasterok, D., and D. Chapman (2011), Heat production and geotherms for the continental lithosphere, *Earth Planet. Sci. Lett.*, *307*(1–2), 59–70, doi:10.1016/j.epsl.2011.04.034.
- Herzberg, C., P. D. Asimow, N. Arndt, Y. Niu, C. M. Leshner, J. G. Fitton, M. J. Cheadle, and A. D. Saunders (2007), Temperatures in ambient mantle and plumes: Constraints from basalts, picrites, and komatiites, *Geochem. Geophys. Geosyst.*, *8*, Q02006, doi:10.1029/2006GC001390.
- Hirth, G., and D. L. Kohlstedt (1996), Water in the oceanic upper mantle: Implications for rheology, melt extraction and the evolution of the lithosphere, *Earth Planet. Sci. Lett.*, *144*, 93–108, doi:10.1016/0012-821X(96)00154-9.
- Holland, T. J. B., and R. Powell (1998), An internally consistent thermodynamic dataset for phases of petrological interest, *J. Metamorph. Geol.*, *16*, 309–343, doi:10.1111/j.1525-1314.1998.00140.x.
- Ionov, D. (2002), Mantle structure and rifting processes in the Baikal-Mongolia region: Geophysical data and evidence from xenoliths in volcanic rocks, *Tectonophysics*, *351*(1–2), 41–60, doi:10.1016/S0040-1951(02)00124-5.
- Jackson, I., and U. H. Faul (2010), Grain-size-sensitive viscoelastic relaxation in olivine: Towards a robust laboratory-based model for seismological application, *Phys. Earth Planet. Inter.*, *183*, 151–163, doi:10.1016/j.pepi.2010.09.005.
- Jackson, I., J. D. Fitz Gerald, U. H. Faul, and B. H. Tan (2002), Grain-size-sensitive seismic wave attenuation in polycrystalline olivine, *J. Geophys. Res.*, *107*(B12), 2360, doi:10.1029/2001JB001225.
- Jaupart, C., and J.-C. Mareschal (2003), Constraints on crustal heat production from heat flow data, in *Treatise of Geochemistry*, vol. 3, *The Crust*, edited by R. L. Rudnick, pp. 65–84, Elsevier, Amsterdam, doi:10.1016/B0-08-043751-6/03017-6.
- Karato, S. (1993), Importance of anelasticity in the interpretation of seismic tomography, *Geophys. Res. Lett.*, *20*(15), 1623–1626, doi:10.1029/93GL01767.
- Karato, S. (2012), On the origin of the asthenosphere, *Earth Planet. Sci. Lett.*, *321–322*, 95–103, doi:10.1016/j.epsl.2012.01.001.
- Katsura, T., et al. (2004), Olivine-wadsleyite transition in the system $(\text{Mg}, \text{Fe})_2\text{SiO}_4$, *J. Geophys. Res.*, *109*, B02209, doi:10.1029/2003JB002438.
- Kawakatsu, H., P. Kumar, Y. Takei, M. Shinohara, T. Kanazawa, E. Araki, and K. Suyehiro (2009), Seismic evidence for sharp lithosphere–asthenosphere boundaries of oceanic plates, *Science*, *324*, 499–502.
- Kennett, B. L. N., E. R. Engdahl, and R. Buland (1995), Constraints on seismic velocities in the Earth from traveltimes, *Geophys. J. Int.*, *122*(1), 108–124, doi:10.1111/j.1365-246X.1995.tb03540.x.
- Kern, H., L. Burlini, and I. V. Ashchepkov (1996), Fabric-related seismic anisotropy in upper-mantle xenoliths: Evidence from measurements and calculations, *Phys. Earth Planet. Inter.*, *95*(3–4), 195–209, doi:10.1016/0031-9201(95)03126-X.
- Khan, A., L. Boschi, and J. A. D. Connolly (2009), On mantle chemical and thermal heterogeneities and anisotropy as



- mapped by inversion of global surface wave data, *J. Geophys. Res.*, *114*, B09305, doi:10.1029/2009JB006399.
- Khan, A., L. Boschi, and J. A. D. Connolly (2011), Mapping the Earth's thermochemical and anisotropic structure using global surface wave data, *J. Geophys. Res.*, *116*, B01301, doi: 10.1029/2010JB007828.
- Khutorskoy, M. D., and V. V. Yarmoluk (1989), Heat flow, structure and evolution of the lithosphere of Mongolia, *Tectonophysics*, *164*(2–4), 315–322, doi:10.1016/0040-1951(89)90024-3.
- Kind, R., X. Yuan, and P. Kumar (2012), Seismic receiver functions and the lithosphere-asthenosphere boundary, *Tectonophysics*, *536–537*, 25–43, doi:10.1016/j.tecto.2012.03.005.
- Kiselev, A. I. (1987), Volcanism of the Baikal Rift zone, *Tectonophysics*, *143*, 235–244, doi:10.1016/0040-1951(87)90093-X.
- Klemme, S. (2004), The influence of Cr on the garnet–spinel transition in the Earth's mantle: Experiments in the system MgO–Cr₂O₃–SiO₂ and thermodynamic modelling, *Lithos*, *77*, 639–646, doi:10.1016/j.lithos.2004.03.017.
- Koulakov, I., and N. Bushenkova (2010), Upper mantle structure beneath the Siberian craton and surrounding areas based on regional tomographic inversion of P and PP travel times, *Tectonophysics*, *486*, 81–100, doi:10.1016/j.tecto.2010.02.011.
- Lachenbruch, A. H., and P. Morgan (1990), Continental extension, magmatism and elevation; formal relations and rules of thumb, *Tectonophysics*, *174*, 39–62.
- Lebedev, S., and R. D. van der Hilst (2008), Global upper-mantle tomography with the automated multimode inversion of surface and S-wave forms, *Geophys. J. Int.*, *173*, 505–518, doi:10.1111/j.1365-246X.2008.03721.x.
- Lebedev, S., S. Chevrot, and R. D. van der Hilst (2003), Correlation between the shear-speed structure and thickness of the mantle transition zone, *Phys. Earth Planet. Inter.*, *136*, 25–40, doi:10.1016/S0031-9201(03)00020-7.
- Lebedev, S., T. Meier, and R. D. van der Hilst (2006), Asthenospheric flow and origin of volcanism in the Baikal Rift area, *Earth Planet. Sci. Lett.*, *249*(3–4), 415–424, doi:10.1016/j.epsl.2006.07.007.
- Lebedev, S., J. Boonen, and J. Trampert (2009), Seismic structure of Precambrian lithosphere: New constraints from broadband surface-wave dispersion, *Lithos*, *109*, 96–111, doi:10.1016/j.lithos.2008.06.010.
- Liu, H.-P., D. L. Anderson, and H. Kanamori (1976), Velocity dispersion due to anelasticity: Implications for seismology and mantle composition, *Geophys. J. R. Astron. Soc.*, *47*, 41–58, doi:10.1111/j.1365-246X.1976.tb01261.x.
- Logatchev, N., and Y. Zorin (1987), Evidence and causes of the two-stage development of the Baikal Rift, *Tectonophysics*, *143*(1–3), 225–234, doi:10.1016/0040-1951(87)90092-8.
- Lysak, S. (1984), Terrestrial heat flow in the south of East Siberia, *Tectonophysics*, *103*(1–4), 205–215, doi:10.1016/0040-1951(84)90084-2.
- Lysak, S. (1995), Terrestrial heat and temperatures in the upper crust in south east Siberia, *Bull. Cent. Rech. Explor. Prod. Elf Aquitaine*, *19*, 39–58.
- Lysak, S., and R. Dorofeeva (2003), Thermal state of the lithosphere in Mongolia, *Russ. Geol. Geophys.*, *44*(9), 893–903.
- McCarthy, C., Y. Takei, and T. Hiraga (2011), Experimental study of attenuation and dispersion over a broad frequency range: 2. The universal scaling of polycrystalline materials, *J. Geophys. Res.*, *116*, B09207, doi:10.1029/2011JB008384.
- McDonough, W. F., and S. S. Sun (1995), The composition of the Earth, *Chem. Geol.*, *120*(3–4), 223–253, doi:10.1016/0009-2541(94)00140-4.
- Minster, B., and D. L. Anderson (1981), A model of dislocation controlled rheology for the mantle, *Philos. Trans. R. Soc. London, Ser. A*, *299*, 319–356, doi:10.1098/rsta.1981.0025.
- Molnar, P., and P. Tapponnier (1975), Cenozoic tectonics of Asia: Effect of a continental collision, *Science*, *189*, 419–425.
- Montagner, J.-P. (2007), Upper mantle Structure: Global isotropic and anisotropic tomography, in *Treatise on Geophysics*, vol. 1, *Seismology and Structure of the Earth* edited by A. M. Dziewonski and B. Romanowicz, pp. 559–590, Elsevier, Amsterdam.
- Muller, M. R., et al. (2009), Lithospheric structure, evolution and diamond prospectivity of the Rehoboth Terrane and western Kaapvaal Craton, southern Africa: Constraints from broadband magnetotellurics, *Lithos*, *112*, 93–105, doi:10.1016/j.lithos.2009.06.023.
- Nickel, K. G., and D. H. Green (1985), Empirical geothermobarometry for garnet peridotites and implication for the nature of lithosphere, kimberlites and diamonds, *Earth Planet. Sci. Lett.*, *73*, 158–170, doi:10.1016/0012-821X(85)90043-3.
- Nielsen, C., and H. Thybo (2009), No Moho uplift below the Baikal Rift zone: Evidence from a seismic refraction profile across southern Lake Baikal, *J. Geophys. Res.*, *114*, B08306, doi:10.1029/2008JB005828.
- Perry, H. K. C., A. M. Forte, and D. W. S. Eaton (2003), Upper-mantle thermochemical structure below North America from seismic-geodynamic flow models, *Geophys. J. Int.*, *154*(2), 279–299, doi:10.1046/j.1365-246X.2003.01961.x.
- Petit, C., and J. Déverchère (2006), Structure and evolution of the Baikal Rift: A synthesis, *Geochem. Geophys. Geosyst.*, *7*, Q11016, doi:10.1029/2006GC001265.
- Petit, C., E. Burov, and J. Déverchère (1997), On the structure and mechanical behaviour of the extending lithosphere in the Baikal Rift from gravity modelling, *Earth Planet. Sci. Lett.*, *149*(1–4), 29–42, doi:10.1016/S0012-821X(97)00067-8.
- Petit, C., J. Déverchère, E. Calais, V. San'kov, and D. Fairhead (2002), Deep structure and mechanical behavior of the lithosphere in the Hangai-Hövsgöl region, Mongolia: New constraints from gravity modelling, *Earth Planet. Sci. Lett.*, *197*(3–4), 133–149, doi:10.1016/S0012-821X(02)00470-3.
- Plomerová, J., D. Kouba, and V. Babuska (2002), Mapping the lithosphere–asthenosphere boundary through changes in surface-wave anisotropy, *Tectonophysics*, *358*, 175–185, doi:10.1016/S0040-1951(02)00423-7.
- Poort, J., and J. Klerkx (2004), Absence of a regional surface thermal high in the Baikal Rift; new insights from detailed contouring of heat flow anomalies, *Tectonophysics*, *383*(3–4), 217–241, doi:10.1016/j.tecto.2004.03.011.
- Priestley, K., and D. McKenzie (2006), The thermal structure of the lithosphere from shear wave velocities, *Earth Planet. Sci. Lett.*, *244*(1–2), 285–301, doi:10.1016/j.epsl.2006.01.008.
- Romanowicz, B. (1995), A global tomographic model of shear attenuation in the upper mantle, *J. Geophys. Res.*, *100*, 12,375–12,394, doi:10.1029/95JB00957.
- Romanowicz, B. (2009), The thickness of tectonic plates, *Science*, *324*(5926), 474–476, doi:10.1126/science.1172879.
- Rudnick, R. L., and D. M. Fountain (1995), Nature and composition of the continental crust: A lower crustal perspective, *Rev. Geophys.*, *33*(3), 267–309, doi:10.1029/95RG01302.
- Rudnick, R. L., W. F. McDonough, and R. J. O'Connell (1998), Thermal structure, thickness and composition of continental

- lithosphere, *Chem. Geol.*, 145(3–4), 395–411, doi:10.1016/S0009-2541(97)00151-4.
- Ruppel, C. (1995), Extensional processes in continental lithosphere, *J. Geophys. Res.*, 100(B12), 24,187–24,215, doi:10.1029/95JB02955.
- Rychert, C. A., and P. M. Shearer (2009), A global view of the lithosphere-asthenosphere boundary, *Science*, 324(5926), 495–498, doi:10.1126/science.1169754.
- Schmerr, N. (2012), The Gutenberg discontinuity: Melt at the lithosphere-asthenosphere boundary, *Science*, 335(6075), 1480–1483, doi:10.1126/science.1215433.
- Selby, N. D., and J. H. Woodhouse (2002), The Q structure of the upper mantle: Constraints from Rayleigh wave amplitudes, *J. Geophys. Res.*, 107(B5), 2097, doi:10.1029/2001JB000257.
- Sengör, A. M. C., and K. Burke (1978), Relative timing of rifting and volcanism on Earth and its tectonic implications, *Geophys. Res. Lett.*, 5(6), 419–421, doi:10.1029/GL005i006p00419.
- Shapiro, N. M., and M. H. Ritzwoller (2004), Thermodynamic constraints on seismic inversions, *Geophys. J. Int.*, 157(3), 1175–1188, doi:10.1111/j.1365-246X.2004.02254.x.
- Simmons, N. A., A. M. Forte, L. Boschi, and S. P. Grand (2010), GyPSuM: A joint tomographic model of mantle density and seismic wave speeds, *J. Geophys. Res.*, 115, B12310, doi:10.1029/2010JB007631.
- Smith, W. H. F., and D. T. Sandwell (1994), Bathymetric prediction from dense satellite altimetry and sparse shipboard bathymetry, *J. Geophys. Res.*, 99(B11), 21,803–21,824, doi:10.1029/94JB00988.
- Smith, W. H. F., and D. T. Sandwell (1997), Global sea floor topography from satellite altimetry and ship depth soundings, *Science*, 277(5334), 1956–1962, doi:10.1126/science.277.5334.1956.
- Sobolev, S. V., H. Zeyen, G. Stoll, F. Werling, R. Altherr, and K. Fuchs (1996), Upper mantle temperatures from teleseismic tomography of French Massif Central including effects of composition, mineral reactions, anharmonicity, anelasticity and partial melt, *Earth Planet. Sci. Lett.*, 139, 147–163, doi:10.1016/0012-821X(95)00238-8.
- Solomatov, V. S., and L. Moresi (2000), Scaling of time-dependent stagnant lid convection: Application to small-scale convection on the Earth and other terrestrial planets, *J. Geophys. Res.*, 105, 21,795–21,817, doi:10.1029/2000JB900197.
- Stixrude, L., and C. Lithgow-Bertelloni (2005), Mineralogy and elasticity of the oceanic upper mantle: Origin of the low-velocity zone, *J. Geophys. Res.*, 110, B03204, doi:10.1029/2004JB002965.
- Stosch, H. G., D. A. Ionov, I. S. Puchtel, S. J. G. Galer, and A. Sharpouri (1995), Lower crustal xenoliths from Mongolia and their bearing on the nature of the deep crust beneath central Asia, *Lithos*, 36(3–4), 227–242, doi:10.1016/0024-4937(95)00019-4.
- ten Brink, U. S., and M. H. Taylor (2002), Crustal structure of central Lake Baikal: Insights into intracontinental rifting, *J. Geophys. Res.*, 107(B7), 2132, doi:10.1029/2001JB000300.
- Tiberi, C., M. Diament, J. Déverchère, C. Petit-Mariani, V. Mikhailov, S. Tikhotsky, and U. Achauer (2003), Deep structure of the Baikal Rift zone revealed by joint inversion of gravity and seismology, *J. Geophys. Res.*, 108(B3), 2133, doi:10.1029/2002JB001880.
- Turcotte, D. L., and G. Schubert (2002), *Geodynamics*, 2nd ed., 456 pp., Cambridge Univ. Press, Cambridge, U. K.
- Ukhanov, A. B., I. D. Ryabchikov, and A. D. Kharkiv (Eds.) (1988), *Lithospheric Mantle of the Yakutian Kimberlite Province*, 286 pp., Nauka, Moscow.
- Vilà, M., M. Fernández, and I. Jiménez-Munt (2010), Radiogenic heat production variability of some common lithological groups and its significance to lithospheric thermal modeling, *Tectonophysics*, 490(3–4), 152–164, doi:10.1016/j.tecto.2010.05.003.
- Wessel, P., and W. H. F. Smith (1995), New version of the Generic Mapping Tools released, *Eos Trans. AGU*, 76, 329.
- Yuan, H., and B. Romanowicz (2010), Lithospheric layering in the North American craton, *Nature*, 466, 1063–1068, doi:10.1038/nature09332.
- Zaronek, S. E., and E. M. Parmentier (2004), The onset of convection in fluids with strongly temperature-dependent viscosity cooled from above with implications for planetary lithospheres, *Earth Planet. Sci. Lett.*, 224, 371–386, doi:10.1016/j.epsl.2004.05.013.
- Zhao, D., J. Lei, T. Inoue, A. Yamada, and S. S. Gao (2006), Deep structure and origin of the Baikal Rift zone, *Earth Planet. Sci. Lett.*, 243, 681–691, doi:10.1016/j.epsl.2006.01.033.
- Zlotnik, S., J. C. Afonso, P. Díez, and M. Fernández (2008), Small-scale gravitational instabilities under the oceans: Implications for the evolution of oceanic lithosphere and its expression in geophysical observables, *Philos. Mag.*, 88, 3197–3217, doi:10.1080/14786430802464248.
- Zorin, Y. (1981), The Baikal Rift: An example of the intrusion of asthenospheric material into the lithosphere as the cause of disruption of lithospheric plates, *Tectonophysics*, 73(1–3), 91–104, doi:10.1016/0040-1951(81)90176-1.
- Zorin, Y. A., V. V. Mordvinova, E. K. Turutanov, B. G. Belichenko, A. A. Artemyev, G. L. Kosarev, and S. S. Gao (2002), Low seismic velocity layers in the Earth's crust beneath eastern Siberia (Russia) and central Mongolia: Receiver function data and their possible geological implication, *Tectonophysics*, 359(3–4), 307–327, doi:10.1016/S0040-1951(02)00531-0.